Nano Research

ISSN 1998-0124 CN 11-5974/O4
https://doi.org/10.26599/NR.2026.94908840

Research Article

Ti_3C_2 MXene folded nanosheets with $Co(OH)_2$ integrated on carbon cloth for enhanced oxygen evolution performance

Bingbing Hang[1], Xilin Zhang[1,2], Qingfang Chang[1,2](✉), Runmin Li[3], Qian Bai[3], Shuai Li[4](✉), Xi Liu[5], Jiajing Pei[5](✉)

[1] School of Physics, Henan Normal University, Xinxiang 453007, China

[2] Key Laboratory of Yellow River and Huai River Water Environmental and Pollution Control, Ministry of Education, School of Environment, Henan Normal University, Xinxiang 453007, China

[3] Energy & Catalysis Center, School of Materials Science and Engineering, Beijing Institute of Technology, Beijing 100081, China

[4] College of Environmental Science and Engineering, North China Electric Power University, Beijing 102206, China

[5] State Key Laboratory of High-efficiency Utilization of Coal and Green Chemical Engineering, College of Chemistry and Chemical Engineering, Ningxia University, Yinchuan 750021, China

Nano Res., **Just Accepted Manuscript** • https://doi.org/10.26599/NR.2026.94908840

https://www.sciopen.com/journal/1998-0124 on May. 13, 2026

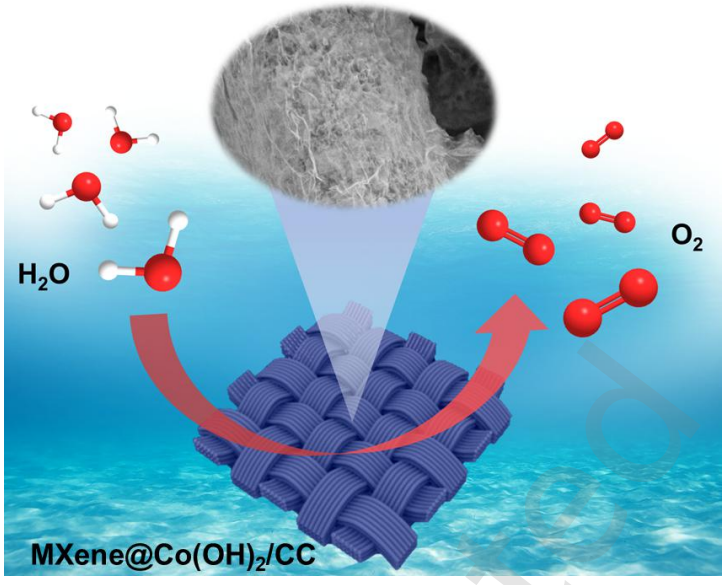

A two-step synthesis route (electrodeposition → soaking → vacuum drying) yields a highly active MXene@$Co(OH)_2$/CC heterostructure electrocatalyst. Electronic coupling at the $Ti_3C_2T_x$ MXene interface triggers local charge redistribution and modifies the electronic states of the active sites, which in turn accelerates charge transport and OER kinetics. The optimal catalyst attains 10 mA cm^{-2} at an overpotential as low as 261 mV, shows a Tafel slope of 61.7 mV dec^{-1}, and maintains stable operation for >1100 h under 10 mA cm^{-2}, making it a promising noble-metal-free candidate for next-generation water electrolysis.

Nano Research

Open Access

Review Article/Research Article Please choose on

Ti_3C_2 MXene folded nanosheets with $Co(OH)_2$ integrated on carbon cloth for enhanced oxygen evolution performance

Bingbing Hang[1], Xilin Zhang[1,2], Qingfang Chang[1,2,*] Runmin Li[3], Qian Bai[3], Shuai Li[4,*], Xi Liu[5], and Jiajing Pei[5,*]

[1] *School of Physics, Henan Normal University, Xinxiang 453007, China*
[2] *Key Laboratory of Yellow River and Huai River Water Environmental and Pollution Control, Ministry of Education, School of Environment, Henan Normal University, Xinxiang 453007, China*
[3] *Energy & Catalysis Center, School of Materials Science and Engineering, Beijing Institute of Technology, Beijing 100081, China*
[4] *College of Environmental Science and Engineering, North China Electric Power University, Beijing 102206, China*
[5] *State Key Laboratory of High-efficiency Utilization of Coal and Green Chemical Engineering, College of Chemistry and Chemical Engineering, Ningxia University, Yinchuan 750021, China*

Received: 6 April 2026; **Revised:** 11 May 2026; **Accepted:** 13 May 2026

Address correspondence to Qingfang Chang, qingfangchang@htu.edu.cn; Shuai Li, 053_lishuai@163.com; Jiajing Pei, pjj@nxu.edu.cn

Cite this article: *Nano Research*, 2026, 19, 94908840 https://doi.org/10.26599/NR.2026.94908840

ABSTRACT: The oxygen evolution reaction (OER) suffers from low intrinsic activity, poor oxidative stability, and insufficient electrical conductivity, which severely limit the practical deployment of non-precious metal electrocatalysts. To overcome these obstacles, we designed an MXene@$Co(OH)_2$ hybrid supported on carbon cloth (MXene@$Co(OH)_2$/CC) using a straightforward electrodeposition and vacuum drying method. Strong interfacial interactions between MXene and $Co(OH)_2$ boost charge transfer, create abundant accessible active sites, and reinforce structural integrity under OER working conditions. Consequently, the MXene@$Co(OH)_2$/CC electrode requires only 261 mV to achieve 10 mA cm^{-2} and shows a Tafel slope of 61.7 mV dec^{-1}, and retains excellent performance for more than 1100 h. Beyond delivering a highly efficient and low-cost OER catalyst, this work also provides a valuable paradigm for constructing well-defined heterostructured catalytic systems via interfacial engineering.

KEYWORDS: $Ti_3C_2T_x$ MXene, oxygen evolution reaction, electrocatalysis, electronic coupling, strong interfacial interaction

1.Introduction

Water electrolysis represents a key technology for producing hydrogen, which is essential for high-energy-density and low-carbon energy systems, thereby tackling the critical challenges of energy scarcity and environmental pollution [1, 2]. Nevertheless, the anodic oxygen evolution reaction (OER) poses a major bottleneck to the overall efficiency of water electrolysis, as it involves a kinetically slow four-electron transfer that incurs high overpotentials and considerable energy losses [3-4]. Precious metal oxides, such as RuO_2, show outstanding intrinsic OER activity, yet their practical application is severely restricted by high cost and limited supply [5-7]. Meanwhile, non-noble metal alternatives often suffer from poor stability under oxidizing conditions, and bubble accumulation at the anode further exacerbates mass transport limitations. Consequently, the development of cost-effective, highly active non-noble metal OER catalysts is of paramount importance [8, 9].

Among various earth-abundant candidates, cobalt-based materials have been extensively explored for the alkaline OER, demonstrating potential to replace precious metal catalysts [10-13] . In particular, $Co(OH)_2$ possesses a distinctive three-dimensional electronic structure and abundant surface -OH groups, which are highly favorable for the alkaline OER ($4OH^- \rightarrow O_2 + 2H_2O + 4e^-$). In strongly alkaline environments, however, $Co(OH)_2$ encounters two major limitations: inadequate electrical conductivity and insufficient active site density. These shortcomings restrict the overall catalytic efficiency of single-component non-precious metal catalysts. [14, 15].

A promising strategy to overcome these limitations involves the construction of heterostructured composites by integrating $Co(OH)_2$ with functional materials such as MXene, graphene, or NiP_x [16-18]. Such heterostructures leverage interfacial coupling effects, which induce local electron redistribution and modulate the electronic structure of the constituent atoms, thereby enhancing electrochemical activity, conductivity, and overall stability [19, 20].

Two-dimensional MXenes (e.g., $Ti_3C_2T_x$ with T_x = -O, -OH, -F) have gained considerable interest as catalyst supports owing to their high electrical conductivity, excellent hydrophilicity, and abundant surface functional groups [21]. The unique properties of MXenes, including their high conductivity and tunable surface chemistry, make them ideal supports for electrocatalysts [22]. The negatively charged surface terminations of MXenes enable efficient electrostatic assembly with positively charged transition metal hydroxides, forming well-defined heterostructures [23, 24].

Such interfacial coupling not only mitigates the self-stacking of MXene layers but also induces local electronic redistribution, thereby enhancing the conductivity and electrocatalytic activity of the hybrid system [16-19] . Furthermore, MXene-based heterostructures have also been explored for environmental applications, including water purification and electrocatalytic pollutant degradation [25].

To address the aforementioned challenges, we report a MXene@$Co(OH)_2$ hybrid integrated onto carbon cloth (CC) via a simple electrodeposition and vacuum drying process. The well-defined heterojunctions formed between $Ti_3C_2T_x$ MXene and $Co(OH)_2$ enable strong electronic coupling and interfacial interaction, which induce local electron redistribution and modulate the electronic structure of the active sites, thereby facilitating efficient charge transfer and accelerating OER kinetics [20]. Consequently, the MXene@$Co(OH)_2$/CC electrode delivers outstanding OER performance with low overpotential, small Tafel slope, and exceptional long-term durability.

Compared with reported MXene/$Co(OH)_2$ OER catalysts, our work has three advantages. First, it delivers over 1100 h of stability, far exceeding the typical 30-100 h (e.g., $Ti_3C_2T_x$/$Co(OH)_2$, 30 h; $Co(OH)_2$/$Mo_2TiC_2T_x$, 100 h) [26-27]. Second, unlike ex-situ XPS, EELS or static XAFS, we use operando XAFS to directly track Co species evolution ($Co(OH)_2$ → CoOOH → Co^{4+}=O) under OER. Third, distinct from conventional hydrothermal or co-precipitation methods, our two-cycle vacuum drying promotes Co-O-Ti bond formation via interfacial dehydration condensation while preserving MXene structure and preventing oxidation. Together, these advances set a new benchmark for MXene/$Co(OH)_2$ OER catalysts.

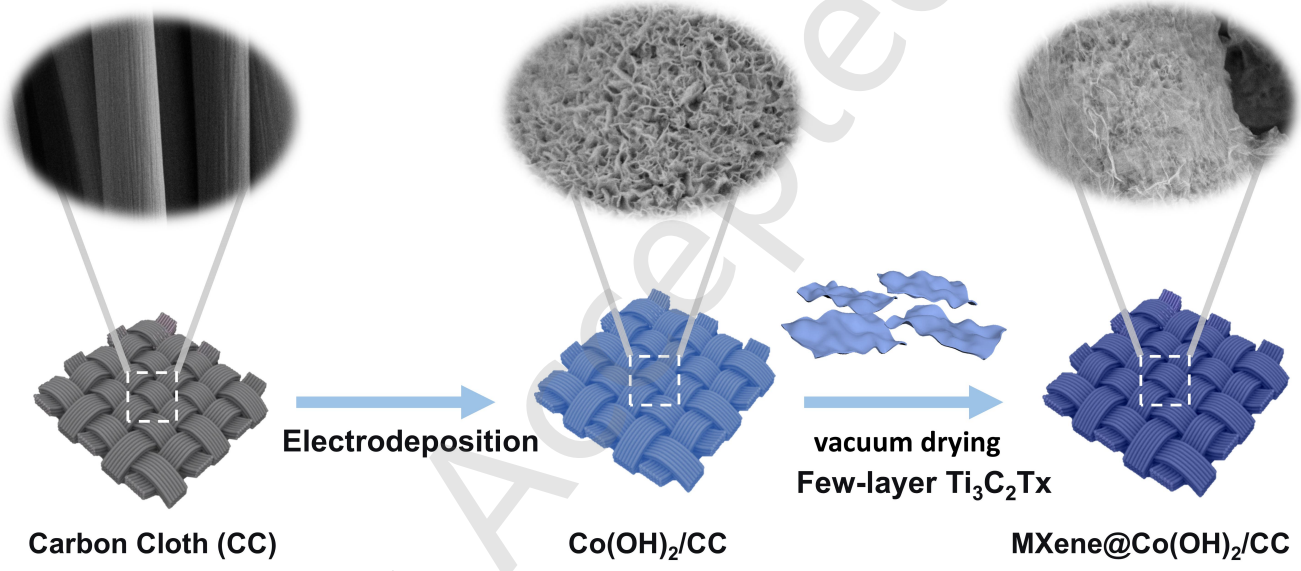

Scheme. 1. Schematic outlining the stepwise construction of the MXene@$Co(OH)_2$/CC composite.

2.Results and discussion

2.1. Characterization of catalysts.

The fabrication of MXene@$Co(OH)_2$/CC involves a two-step process comprising electrodeposition and subsequent vacuum drying. First, $Co(OH)_2$ nanosheet arrays were directly electrodeposited onto acid-pretreated carbon cloth (CC) to obtain $Co(OH)_2$/CC. The as-prepared $Co(OH)_2$/CC was then immersed in a colloidal dispersion of $Ti_3C_2T_x$ MXene nanosheets, followed by vacuum drying, yielding the MXene@$Co(OH)_2$/CC hybrid.

The formation of the heterostructure is primarily driven by electrostatic interactions between the positively charged $Co(OH)_2$ surface and the negatively charged functional groups (e.g., -OH, -O, and -F) present on the MXene nanosheets. Key reaction parameters, including the reaction temperature, were carefully controlled to ensure stable and reproducible composite formation. The temperature and time for vacuum drying after immersion in the MXene dispersion were 80 °C and 15 minutes, respectively. The resulting MXene@$Co(OH)_2$/CC exhibited a well-interconnected network morphology with uniform distribution of $Co(OH)_2$ nanosheets on the MXene-decorated carbon cloth substrate. Notably, subjecting the sample to two cycles of vacuum drying further enhanced the structural integrity and electrochemical performance.

Fig. S1 provides the outcome of morphological and microstructural investigations conducted on the as-fabricated samples utilizing a combination of scanning electron microscopy (SEM) and transmission electron microscopy (TEM); the pristine carbon cloth exhibits a smooth fiber surface, serving as a highly conductive and structurally robust substrate for catalyst growth. After electrodeposition, the $Co(OH)_2$ nanosheets were intimately and uniformly packed onto the surface of the carbon fibers, forming a conformal coating (Fig. S2). It reveals that the nanosheets exhibit a smooth surface and are vertically oriented on the carbon fiber substrate, creating a three-dimensional interconnected network with exposed edges, which facilitates electrolyte infiltration and mass transport.

After the soaking and vacuum drying process, the MXene@$Co(OH)_2$/CC hybrid was obtained (Fig. 1a). To investigate the internal structure, the surface layer was peeled off. Retention of a nanosheet architecture analogous to pristine $Co(OH)_2$/CC is evident from the SEM image (Fig. 1b), where intertwined MXene and $Co(OH)_2$ nanosheets are seen. HRTEM Fig. 1c further demonstrates that MXene nanosheets lie flat on the $Co(OH)_2$ surface, indicating

intimate interfacial contact. In Fig. S3, few-layer MXene flakes are observed in close contact with $Co(OH)_2$ nanosheets, with vertical stripe-like $Co(OH)_2$ lattice fringes visible through transparent MXene layers, pointing to a well-defined heterointerface. The HAADF-STEM image (Fig. 1d) further supports this intimate contact. From the EDS elemental mapping depicted in Fig. 1e, we observe a homogeneous dispersion of C, O, Ti, and Co, which points to a well-integrated structure. Meanwhile, the higher-magnification HRTEM image (Fig. 1f) resolves lattice fringes at distances of 0.221 nm and 0.18 nm; these values match the (301) plane of $Co(OH)_2$ and the (110) plane of $Ti_3C_2T_x$ MXene, respectively. Taken together, these results verify that the MXene@$Co(OH)_2$/CC composite has been successfully formed and that the heterostructure is well defined.

We next employed X-ray diffraction (XRD) to determine the phase composition and crystalline structure. The pattern obtained Fig. S4(a) features distinct peaks attributable to $Co(OH)_2$ (JCPDS No. 46-0605)[28], together with a reflection at 25.6° that originates from the carbon cloth substrate [29-31]. The successful etching of Ti_3AlC_2 to $Ti_3C_2T_x$ MXene was evidenced by the appearance of the characteristic (002) peak at around 6 ° (Fig. S4b), accompanied by the disappearance of the (104) peak of Al at 39 °, indicating complete removal of the Al layers [32]. Notably, upon integration of $Co(OH)_2$, the (002) peak of MXene in the MXene@$Co(OH)_2$/CC composite shifted from 6.1° to 5.3° (Fig. S4c), suggesting an enlarged interlayer spacing of MXene. This shift is attributed to the surface coating of Co^{2+} species derived from $Co(OH)_2$, which effectively inhibits the restacking of MXene layers [33].

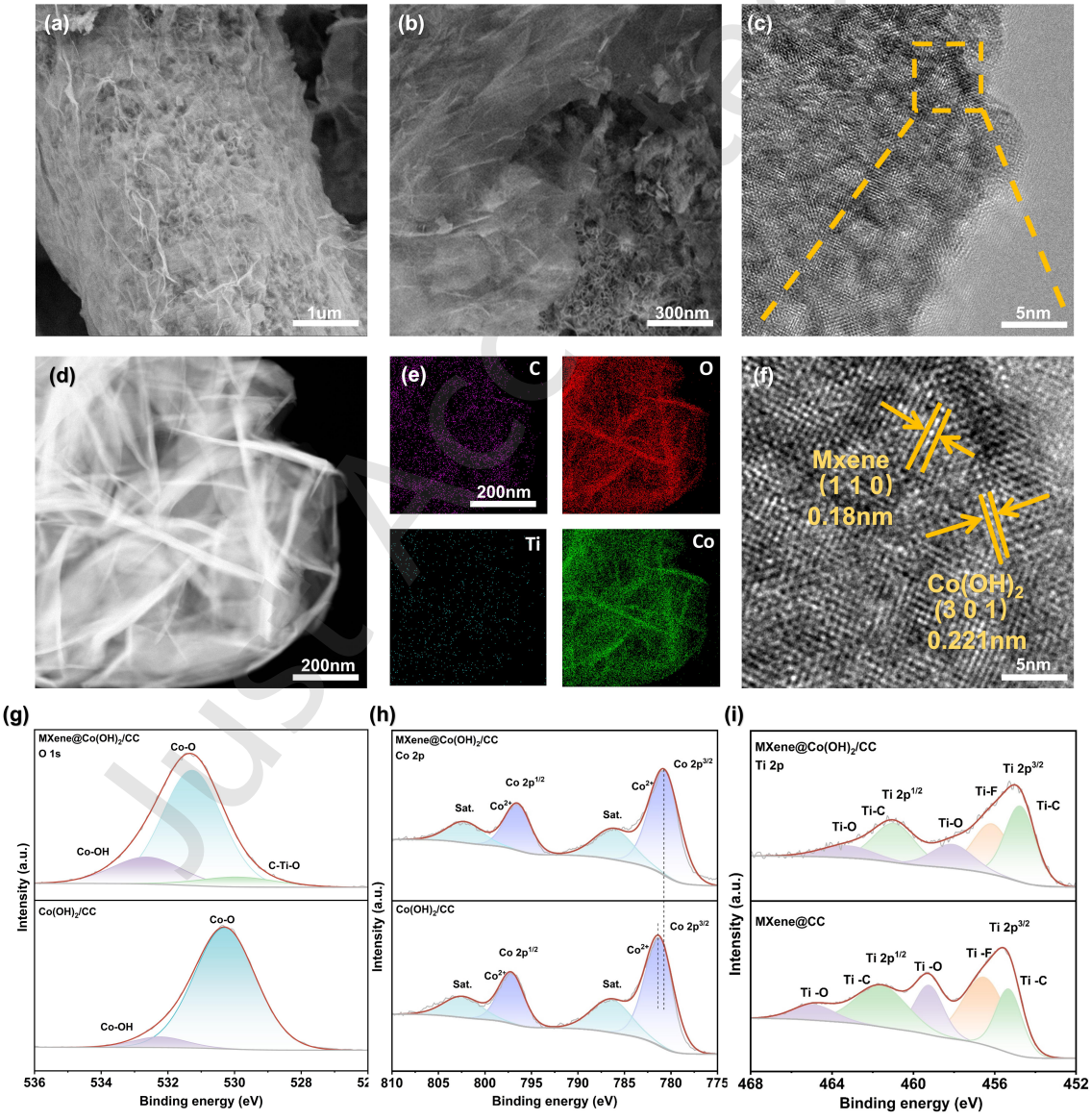

Fig. 1. (a) SEM view of $Co(OH)_2$ supported on carbon cloth (CC); (b) SEM image showing scratched surface features of MXene@$Co(OH)_2$/CC; (c) HRTEM visualization of the MXene@$Co(OH)_2$/CC hybrid; (d) HAADF-STEM image; (e) EDS elemental mapping (C, O, Ti, Co); (f) HRTEM image at higher magnification; (g) O 1s XPS spectrum; (h) Co 2p XPS spectrum; (i) Ti 2p XPS spectrum.

Raman spectroscopy was employed to probe the structural features and interfacial interactions. As shown in Fig. S5a, the Raman spectrum of MXene@$Co(OH)_2$/CC exhibits characteristic peaks at 461.5 cm^{-1} and 525.5 cm^{-1},

corresponding to the E_g and A_{2u} vibrational modes of $Co(OH)_2$, respectively [34]. These two peaks undergo a clear blue shift relative to those of pristine $Co(OH)_2$/CC. This observation suggests two phenomena: the formation of chemical bonds between Co^{2+} and MXene, and the occurrence of charge transfer at the heterojunction interface [35-37]. The Raman spectrum also reveals the characteristic D and G bands of carbonaceous materials at 1355.5 cm^{-1} and 1600.5 cm^{-1}, respectively (Fig. S5b) [38]. For pure $Ti_3C_2T_x$ MXene, the A_1g symmetric out-of-plane vibration and E_g group vibrations were observed at 199.1, 388.5, and 623.8 cm^{-1} (Fig. S4b) [39-40]. XPS analysis was carried out to examine the surface chemistry and electronic interactions of the MXene@$Co(OH)_2$/CC composite. The survey spectrum (Fig. S6a) verifies the coexistence of Co, O, C, Ti, and F, confirming that the two materials are well integrated. The high-resolution C 1s spectrum (Fig. S6b) resolves into three peaks, corresponding to C=O, C–C, and C–Ti bonds. The O 1s spectrum (Fig. 1g) shows three distinct peaks at 529.89, 531.27, and 532.63 eV, assigned to Co–O, C–Ti–O, and Co–OH species [41]. The Co 2p spectrum (Fig. 1h) consists of two main peaks at 781.3 eV (Co $2p_{3/2}$) and 797.1 eV (Co $2p_{1/2}$), along with two satellite peaks at 786.4 and 802.5 eV, all of which are typical for $Co(OH)_2$. Importantly, the Co $2p_{3/2}$ peak of the MXene@$Co(OH)_2$/CC heterostructure is negatively shifted by 0.6 eV relative to that of pristine $Co(OH)_2$/CC, curve fitting of the high-resolution Ti 2p spectrum (Fig. 1i) reveals four component peaks, which are conventionally assigned to Ti–C (454.6 eV), Ti^{2+} (456.1 eV), Ti^{3+} (460.5 eV), and Ti–O (462.2 eV) bonds. respectively. These assignments are consistent with the typical binding energies of Ti 2p in $Ti_3C_2T_x$ MXene systems reported by Halim et al [42]. Notably, the Co 2p peaks exhibit a negative shift (Fig. 1h), indicating an increase in electron density on Co due to electron transfer from MXene to $Co(OH)_2$, whereas the O 1s peaks (particularly Co–O and Co–OH) show a positive shift (Fig. 1g), which is attributed to the formation of Co–O–Ti covalent bonds and the resulting redistribution of electron density away from oxygen atoms. These opposite shift directions are mutually consistent and together confirm the strong interfacial electronic coupling, similar to the interfacial electronic coupling reported for FeOOH/NiFe-LDH (where a Ni–O–Fe bridge bond facilitates charge redistribution) [43] and other MXene/metal hydroxide interfaces [44]. Such interfacial electron transfer contributes to an increased surface charge carrier density of $Co(OH)_2$.

The two-cycle vacuum drying enhances performance via interfacial dehydration condensation. The first drying brings $Co(OH)_2$ and MXene into close contact, while the second drives formation of additional Co–O–Ti bonds. This is supported by XPS (emergence of Co–O–Ti peak and further Co 2p negative shift) and EIS (decreased Rct). The vacuum environment also prevents MXene oxidation (no TiO_2 in Raman), preserving conductivity and surface groups. These synergistic effects improve charge transfer and structural stability, underpinning the superior OER activity and durability.

MXene offers high conductivity, abundant surface –OH/–O/–F groups, 2D confinement, and hydrophilicity, making it an ideal support. Strong interfacial interaction originates from vacuum-driven dehydration condensation between MXene –OH and $Co(OH)_2$, forming Co–O–Ti covalent bonds (XPS evidence). This strategy may be applicable to other hydroxyl-rich supports, though further verification is needed. MXene currently provides the best combination of properties for stable OER catalysis.

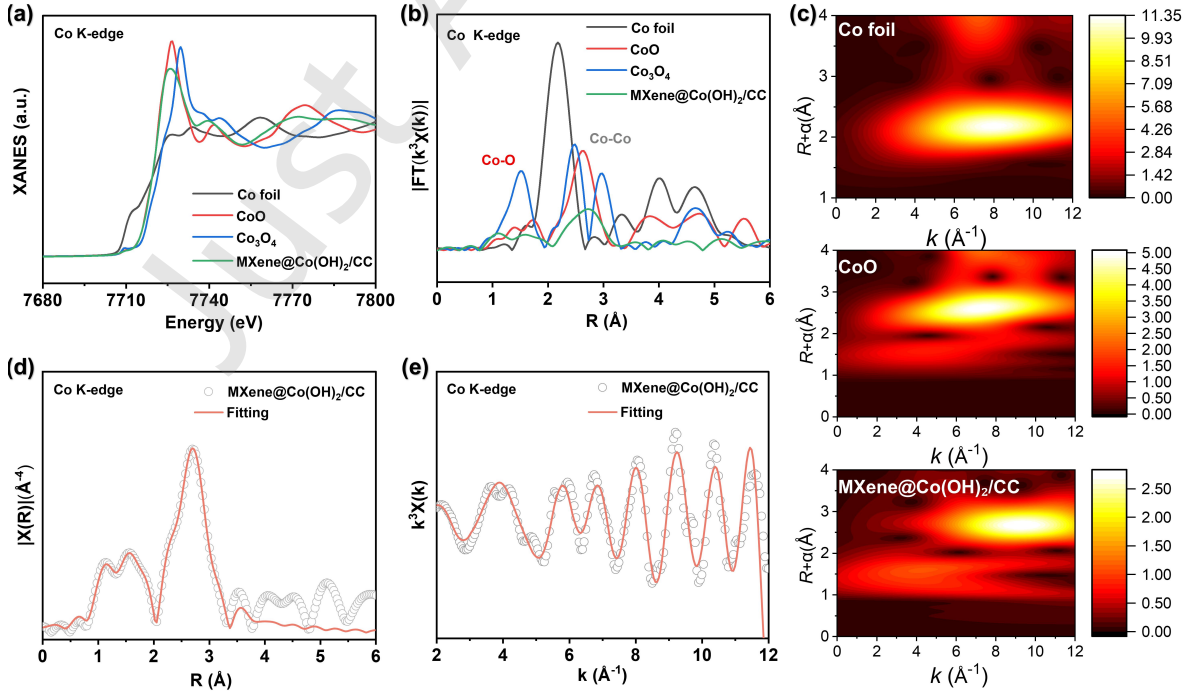

Fig. 2 (a) XANES spectra, (b) FT-EXAFS spectra, (c) WT-EXAFS plots, (d) R-space fitting curves, and (e) k-space fitting curves, confirming the Co^{2+} oxidation state and octahedral Co-O coordination environment.

2.2. Catalytic Active Sites of MXene@$Co(OH)_2$/CC

To probe the electronic structure and local coordination environment of Co active sites in MXene@$Co(OH)_2$/CC, Co K-edge X-ray absorption fine structure (XAFS) measurements were carried out at the BL1W1B beamline of the Beijing Synchrotron Radiation Facility (BSRF). The acquired data were processed and analyzed using the IFEFFIT package [45] and the Demeter software suite (Athena/Artemis) [46] , following standard procedures for background subtraction, normalization, and Fourier transformation. Wavelet transform extended X-ray absorption fine structure (WT-EXAFS) analysis was performed according to the method described by Funke et al [47]. to distinguish overlapping scattering paths (e.g., Co-O vs. Co-Co). Fig. 2a presents the X-ray absorption near-edge structure (XANES) spectrum of MXene@$Co(OH)_2$/CC, which is highly similar to that of the CoO reference. This observation conclusively demonstrates that Co predominantly exists in the +2 oxidation state, which is consistent with the formation of $Co(OH)_2$ via electrodeposition. No detectable signals from metallic Co^0 or Co^{3+} species are observed, attesting to the high phase purity of the as-prepared catalyst.

The FT-EXAFS spectra (Fig. 2b) reveal clear scattering signals from the atomic environment of Co. A prominent peak at around 1.6 Å is assignable to Co–O coordination, whereas the peak at 2.5 Å corresponds to Co-Co metallic bonding. Notably, the Co-Co peak in MXene@$Co(OH)_2$/CC is weak compared with those of Co foil and Co_3O_4, demonstrating the absence of metallic Co clusters and the high dispersion of $Co(OH)_2$ nanosheets. Wavelet-transform (WT)-EXAFS (Fig. 2c and Fig. S10) further distinguishes Co-O and Co-Co contributions in both K-space and R-space, showing a strong intensity for Co-O scattering and barely visible Co-Co paths (Fig. S8). This consolidates the conclusion that Co centers are primarily bonded to O atoms in an octahedral coordination geometry. The combination of EXAFS and wavelet transform has been successfully applied to resolve the coordination environment of atomically dispersed Co on N- doped carbon [48], and we adopt a similar strategy here. Quantitative EXAFS fitting was performed in R-space (Fig. 2d), k-space (Fig. 2e) and q-space (Fig. S7). The experimental data are well reproduced by the fitting curves, validating the reliability of the structural parameters, as confirmed by the control fitting of Co foil (Fig. S9 and Table S1). The fitting results give a Co-O bond length of ≈2.0 Å and a coordination number of ≈6, characteristic of typical $Co(OH)_2$ crystals that are beneficial for OER catalysis. The Co–O bond length (≈2.0 Å) and coordination number (≈6) derived from EXAFS fitting are consistent with the typical octahedral geometry reported for $Co(OH)_2$ [49]. Such a well-defined coordination environment, together with the strong electronic coupling between MXene and $Co(OH)_2$ revealed by XPS and Raman analyses [50] , is consistent with the optimization of the adsorption-desorption energy barriers of OER intermediates and contributes to the reaction kinetics.

2.3. Catalytic Performance.

We evaluated the OER electrocatalytic activity of the prepared catalysts in a 1 M KOH aqueous solution using a standard three-electrode setup. Under the same testing conditions, the MXene@$Co(OH)_2$/CC catalyst demonstrated outstanding OER performance. The linear sweep voltammetry (LSV) curves (Fig. 3a) show that MXene@$Co(OH)_2$/CC needs only 261 mV to reach 10 mA cm^{-2}, far lower than the overpotentials required for $Co(OH)_2$/CC (284 mV) and RuO_2 (319 mV). From the Tafel plots (Fig. 3b), we extracted the Tafel slope, a key parameter reflecting the rate-determining step of the OER. For MXene@$Co(OH)_2$/CC, this value is as low as 61.7 mV dec^{-1}, surpassing those of $Co(OH)_2$/CC (73.9 mV dec^{-1}) and MXene/CC (66.9 mV dec^{-1}). These findings strongly suggest that MXene@$Co(OH)_2$/CC benefits from favorable OER catalytic kinetics.

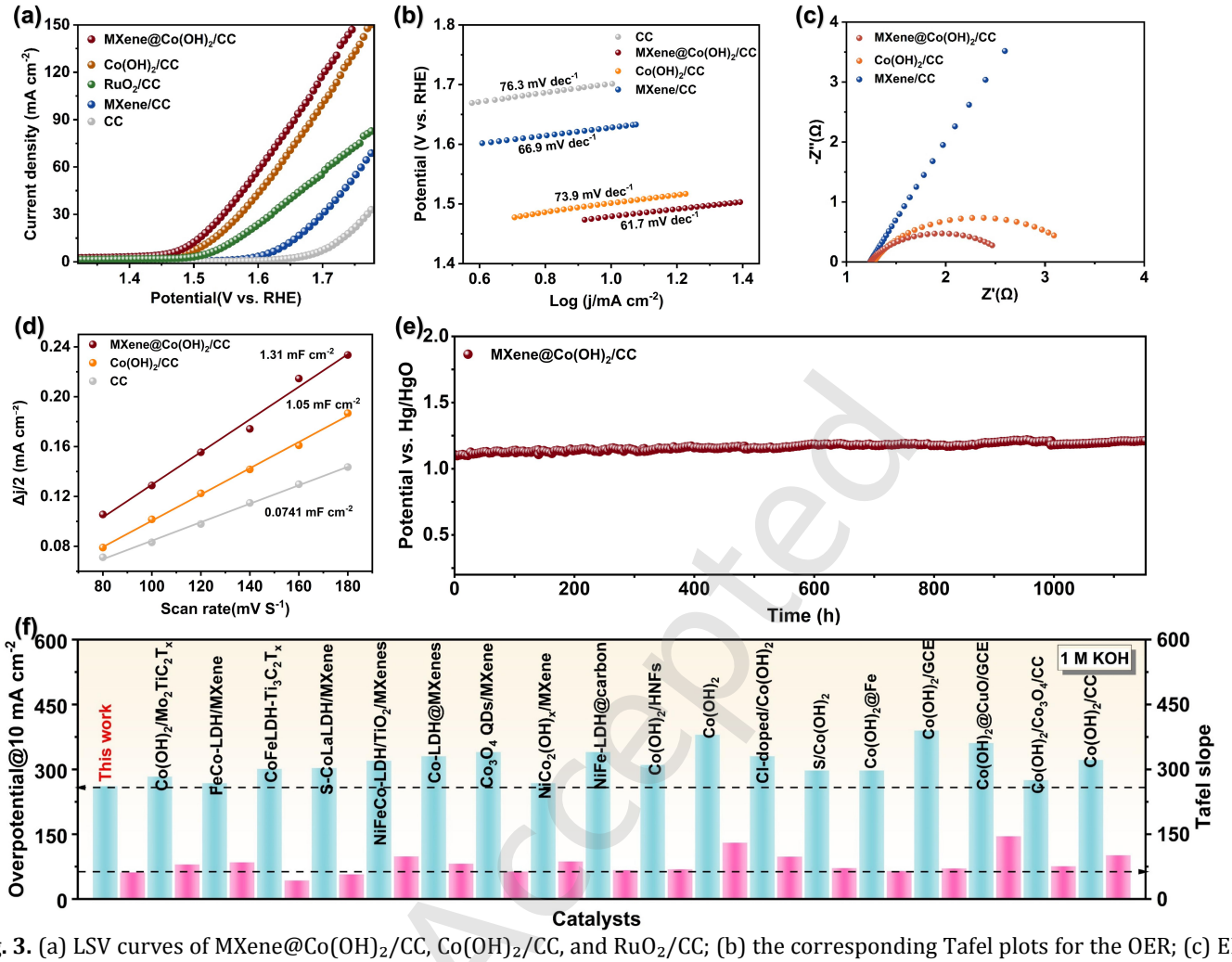

Fig. 3. (a) LSV curves of MXene@$Co(OH)_2$/CC, $Co(OH)_2$/CC, and RuO_2/CC; (b) the corresponding Tafel plots for the OER; (c) EIS plots; (d) Double-layer capacitance (Cdl) plots of MXene@$Co(OH)_2$/CC; (e) Chronopotentiometric stability test of MXene@$Co(OH)_2$/CC at 10 mA cm^{-2} in 1.0 M KOH (100 mL) using a Hg/HgO reference electrode; (f) Comparison of the overpotential at 10 mA cm^{-2} for different catalysts reported in the literature.

Additionally, an assessment of charge transfer can be made via the Nyquist plot shown in (Fig. 3c). The electrochemical impedance spectroscopy (EIS) spectra of MXene@$Co(OH)_2$/CC, $Co(OH)_2$/CC, and MXene/CC demonstrate that the MXene@$Co(OH)_2$/CC composites have superior transfer kinetics, which is ascribed to the introduction of highly conductive MXene. As shown in Table S2, MXene@$Co(OH)_2$/CC only shows a small charge transfer resistance (Rct) of 1.68 Ω, which is lower than those of $Co(OH)_2$/CC (2.188 Ω) and MXene/CC (204.5 Ω), indicating efficient charge transfer kinetics. Electrochemical impedance spectroscopy (EIS) is measured, and the corresponding equivalent circuit and fitted resistance data. The results show that the charge transfer resistance of the $Ti_3C_2T_x$ MXene-containing composite is reduced, which contributes to more efficient electron flow and diffusion kinetics, thereby supporting the enhanced electrocatalytic performance. The double-layer capacitance (Cdl) of MXene@$Co(OH)_2$/CC is 1.31 mF cm^{-2}, which is only marginally higher than that of $Co(OH)_2$/CC (1.05 mF cm^{-2}), as displayed in Fig. 3d. This modest increase suggests that the enhancement in OER activity cannot be attributed solely to an increase in electrochemically active surface area (ECSA). Instead, the improved performance is primarily ascribed to the strong interfacial electronic coupling between MXene and $Co(OH)_2$, as evidenced by the XPS binding-energy shifts, Raman frequency shifts, and operando XAFS-identified evolution of Co species. Collectively, these observations indicate that MXene contributes to the enhanced OER performance through both increased active site exposure and modulated electronic structure of the Co sites, rather than through a purely surface-area effect.

Furthermore, we plotted LSV curves normalized by ECSA based on the impact of ECSA on current density during the catalytic process, as displayed in Fig. S11. The findings reveal that the catalyst possesses high intrinsic oxygen evolution activity per active site, alongside an increased number of active sites [51]. In addition to activity, catalyst stability represents another critical metric for performance evaluation. The stability of MXene@$Co(OH)_2$/CC was assessed using chronopotentiometry without iR-correction compensation. As shown in Fig. 3e, we tested the durability of MXene@$Co(OH)_2$/CC using chronopotentiometry without iR correction, applying a constant current of 10 mA cm^{-2}. The setup included a Hg/HgO reference electrode and 100 mL of 1.0 M KOH.During 1100 h, the machine-recorded raw potential climbed from 0.588 V to 0.632 V (vs. Hg/HgO). Converting these readings to the RHE scale via $E_{RHE} = E_{Hg/HgO} + 0.098 + 0.059 \times 14$ (pH = 14) gave 1.512–1.556 V vs. RHE,

i.e., overpotentials of 282–326 mV. The average potential drift was 0.057 mV h^{-1}. When the electrolyte turned a light yellow during the long-term run, it was replaced with fresh 1.0 M KOH (every few tens of hours approximately). The result shown comes from a single trial without duplicates. Nevertheless, the >1100 h lifetime should be interpreted as a sign of decent stability under the described test conditions, not as a rigorously substantiated exceptional claim. The remarkably good stability of our catalyst outperforming most previously reported Co-based OER electrocatalysts, highlighting the critical role of interfacial stabilization [52]. For comparison, $Co(OH)_2$/CC exhibited a more pronounced increase in overpotential after stability testing in Fig. S12, indicating that MXene@$Co(OH)_2$/CC possesses superior electrochemical stability. The ultra-high stability (>1100 h) of MXene@$Co(OH)_2$/CC originates from three synergistic factors based on research consensus. Interfacial interaction: strong Co-O-Ti covalent bonding anchors $Co(OH)_2$ onto MXene, preventing detachment and aggregation. Structural confinement: 2D MXene nanosheets physically confine $Co(OH)_2$, preserving the nanosheet morphology and heterointerface during prolonged operation. Electronic stabilization: MXene acts as an electron reservoir, stabilizing Co^{3+}/Co^{4+} species within the optimal oxidation state range (+2.8 to +3.0) and preventing over-oxidation to soluble Co^{4+}. Together, these factors-strong bonding, physical confinement, and electronic buffering-synergistically ensure the exceptional durability of the catalyst.

Based on the LSV curves of MXene@$Co(OH)_2$/CC samples with varying electrodeposition times, as depicted in Fig. S13, the MXene@Co(OH)/CC-1200s sample deposited for 20 minutes exhibits the best performance. Electrochemical activity is also reflected in the Tafel slope value; a smaller slope indicates more rapid response kinetics. The addition of $Co(OH)_2$ dramatically decreased the Tafel slope, as seen in Fig.3b. The Tafel slope of MXene@$Co(OH)_2$/CC-1200s dropped to 61.1 mV dec^{-1} compared to $Co(OH)_2$/CC (70.4 mV dec^{-1}), showing enhanced oxygen evolution reaction efficiency of the MXene@$Co(OH)_2$/CC heterostructure. A fair performance assessment was carried out by comparing the OER activity of MXene@$Co(OH)_2$/CC with that of commercial RuO_2 and various recently reported non-precious metal OER catalysts. All electrochemical tests were performed under identical measurement protocols: 1.0 M KOH, carbon cloth as the working electrode substrate, no iR compensation, and normalization based on geometric current density. Fig. 3f and table S3 summarize the results: MXene@$Co(OH)_2$/CC requires only 261 mV to deliver 10 mA cm^{-2}. This value is 58 mV lower than that measured for RuO_2 (319 mV) and also surpasses the values reported for most advanced Co-based OER electrocatalysts. These observations conclusively prove that our heterostructure catalyst exhibits superior intrinsic OER activity under well-matched testing conditions. Therefore, this composite represents a highly promising, noble-metal-free candidate for efficient oxygen evolution in 1.0 M KOH.

To assess the morphological, structural and chemical evolution of MXene@$Co(OH)_2$/CC after 1100 hours of continuous OER catalysis, post-stability SEM, TEM and XPS characterizations were carried out.

As presented in Fig. S14, the composite maintains its well-defined nanosheet-based hierarchical architecture, without observable structural collapse, particle aggregation, or exfoliation from the underlying carbon cloth substrate. The HRTEM image Fig. S15 further confirms the preservation of distinct lattice fringes for both $Co(OH)_2$ and $Ti_3C_2T_x$ MXene, demonstrating the robust structural integrity and strong interfacial interaction of the composite. In addition, the high-resolution XPS spectra of O 1s, Co 2p and C 1s Fig. S16 verify that the chemical states and surface functional groups of the electrode remain largely unaltered after the long-term test. These findings collectively establish the exceptional structural and compositional stability of MXene@$Co(OH)_2$/CC under harsh alkaline OER operating conditions.

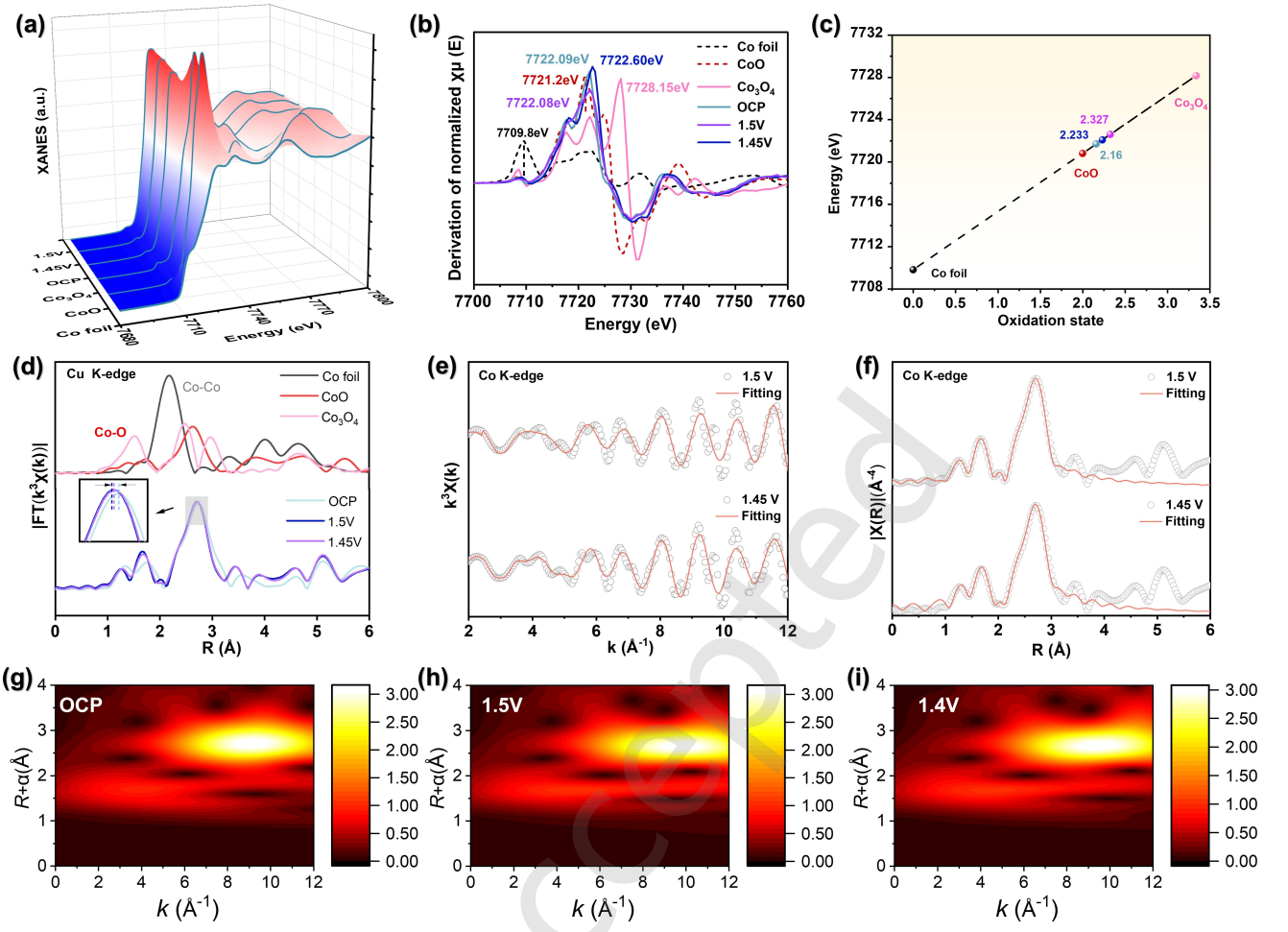

Fig. 4. In-situ Co K-edge XAFS analysis of MXene@Co(OH)$_2$/CC under OER conditions: (a) 3D XANES plot; (b) derivative XANES spectra; (c) oxidation state evolution; (d) Fourier-transform EXAFS (FT-EXAFS) spectra, (e) fitting results in k-space; (f) fitting results in R-space; and (g-i) WT-EXAFS plots at different potentials.

2.4. In-situ Co K-edge XAFS Analysis under OER Conditions

The three-dimensional XANES plot (Fig. 4a) and its first derivatives (Fig. 4b) reveal a progressive shift of the absorption edge toward higher energies with increasing applied potential, indicating partial oxidation of Co^{2+} to higher valence states (Co^{3+}/Co^{4+}) under OER conditions. Concurrently, the white-line intensity increases, suggesting enhanced orbital hybridization between Co and O atoms. A linear calibration of edge energy against oxidation state (Fig. 4c) yields average Co oxidation states of 2.233 at 1.45 V and 2.327 at 1.50 V, approaching that of Co_3O_4. The formation of Co^{4+} species at a relatively low overpotential (1.50 V vs. RHE) suggests that the interfacial coupling between MXene and Co(OH)$_2$ facilitates the reconstruction process, similar to the promoting effect of adsorbed chromate on NiFe-LDH [53]. This trend is consistent with the formation of highly active oxyhydroxide intermediates during OER.

Fourier-transformed EXAFS (FT-EXAFS) spectra (Fig. 4d) show that the Co-O coordination peak at ≈1.6 Å remains dominant across all potentials, while the Co-Co metallic peak at ≈2.5 Å is negligible. This confirms the persistence of the octahedral Co-O coordination environment even under strongly oxidative conditions. The inset enlargement further reveals a slight contraction of the Co-O bond length with increasing potential, consistent with the formation of higher-valent Co species. Quantitative EXAFS fitting was performed in both k-space (Fig. 4e and Fig. S17) and R-space (Fig. 4f) for the spectra acquired at 1.5 V and 1.45 V. The experimental data (open circles) are well reproduced by the fitting curves (red solid lines) (Fig. S18), validating the extracted structural parameters. The fitting results indicate a slight decrease in Co-O bond length (from ≈1.94 Å to ≈1.90 Å).

Wavelet-transform (WT) EXAFS plots (Fig. 4g-i) further confirm the exclusive presence of Co-O scattering paths across all potentials, with no detectable Co-Co metallic signals. This finding demonstrates that the Co active sites remain highly dispersed without aggregation or metallic cluster formation during OER, preserving the structural integrity and stability of the catalyst.

Collectively, these in-situ XAFS results reveal that the Co active sites undergo a reversible valence evolution from Co^{2+} to a mixed Co^{2+}/Co^{3+} state under OER potentials, while retaining the favorable octahedral Co-O coordination environment and structural robustness. Analogous to the surface reconstruction observed in NiFe-LDH upon boron modification [54], our operando XAFS reveals a potential-driven transformation of Co(OH)$_2$ to CoOOH and further to high-valence Co^{4+}, which is identified as the true active phase for OER. Such a flexible structural rearrangement reduces the energy penalty associated with

the uptake and release of OER intermediates, and it is also responsible for the high catalytic activity and long-term stability observed for MXene@$Co(OH)_2$/CC.

3. Conclusions

In conclusion, a highly efficient electrocatalyst featuring a MXene@$Co(OH)_2$/CC heterostructure has been developed via the assembly of conductive MXene nanosheets onto $Co(OH)_2$ arrays pre-deposited on a carbon cloth substrate. The pronounced interfacial coupling between $Co(OH)_2$ and MXene elicits local electron reallocation and alters the electronic environment of the active sites, thereby contributing to efficient charge transfer and favorable OER kinetics. Meanwhile, the introduction of the conductive carbon cloth and MXene not only enhances the electrical conductivity of $Co(OH)_2$ but also stabilizes its nanostructure against aggregation. These synergistic features provide the MXene@$Co(OH)_2$/CC composite with superior electron transport capability and abundant accessible active sites. The optimized catalyst delivers OER activity: an overpotential 261 mV is required to reach 10 mA cm^{-2}, and the Tafel slope is 61.7 mV dec^{-1}. It also exhibits long-term stability, exceeding 1100 h under the described test conditions, which positions it as a promising candidate for future water electrolysis applications.

Supporting Information

Supporting Information is available from the Wiley Online Library or from the author.

Acknowledgements

This work was financially supported by the National Natural Science Foundation of China (Nos. U180413, 11904084, andU2004212) and Center for Outstanding Overseas Scientists (No. GZS2023007).

Conflict of interest

The authors declare no competing interests.

Data Availability Statement

The data that support the findings of this study are available from the corresponding author upon reasonable request.

References

[1] Yang H, Zhang Y, Hu F, et al. Urchin-like CoP nanocrystals as hydrogen evolution reaction and oxygen reduction reaction dual-electrocatalyst with superior stability[J]. *Nano letters*, 2015, *15(11): 7616-7620.*

[2] Li R, Zhou D, Luo J, et al. The urchin-like sphere arrays Co_3O_4 as a bifunctional catalyst for hydrogen evolution reaction and oxygen evolution reaction[J]. *Journal of Power Sources,* 2017, *341: 250-256.*

[3] Yin Q, Tan J M, Besson C, et al. A fast soluble carbon-free molecular water oxidation catalyst based on abundant metals[J]. *Science,* 2010, *328(5976): 342-345.*

[4] Xie L, Zhang R, Cui L, et al. High‐performance electrolytic oxygen evolution in neutral media catalyzed by a cobalt phosphate nanoarray[J]. *Angewandte Chemie International Edition,* 2017, *56(4): 1064-1068.*

[5] Lee Y, Suntivich J, May K J, et al. Synthesis and activities of rutile IrO2 and RuO2 nanoparticles for oxygen evolution in acid and alkaline solutions [J]. *The journal of physical chemistry letters,* 2012, *3(3): 399-404.*

[6] Cherevko S, Geiger S, Kasian O, et al. Oxygen and hydrogen evolution reactions on Ru, RuO2, Ir, and IrO2 thin film electrodes in acidic and alkaline electrolytes: A comparative study on activity and stability[J]. *Catalysis Today*, 2016, *262: 170-180.*

[7] Reier T, Oezaslan M, Strasser P. Electrocatalytic oxygen evolution reaction (OER) on Ru, Ir, and Pt catalysts: a comparative study of nanoparticles and bulk materials[J]. *Acs Catalysis*, 2012, *2(8): 1765-1772.*

[8] Zhang J, Wang T, Pohl D, et al. Interface engineering of MoS2/Ni3S2 heterostructures for highly enhanced electrochemical overall‐water‐splitting activity[J]. *Angewandte Chemie,* 2016, *128(23): 6814-6819.*

[9] Peng L, Nie Y, Zhang L, et al. Self‐assembly‐and Preshaping‐assisted Synthesis of Molybdenum Carbide Supported on Ultrathin Nitrogen‐doped Graphitic Carbon Lamellas for the Hydrogen Evolution Reaction[J]. *ChemCatChem,* 2017, *9(9): 1588-1593.*

[10] Kim D H, Lee Y K. Understanding highly active and durable Fe-decorated $Co(OH)_2$ catalysts in alkaline oxygen evolution reaction by in situ XANES studies[J]. *Chemical Engineering Journal,* 2024, *490: 151701.*

[11] Zheng J, Hu G, Liu B, et al. In-situ spatial-embedding construction of FeCo nucleus-bound carbon skeletons for durable rechargeable liquid and flexible Zn-air batteries[J]. *Energy Storage Materials,* 2024, *65: 103106.*

[12] Gerken J B, McAlpin J G, Chen J Y C, et al. Electrochemical water oxidation with cobalt-based electrocatalysts from pH 0–14: the thermodynamic basis for catalyst structure, stability, and activity[J]. *Journal of the American Chemical Society,* 2011, *133(36): 14431-14442.*

[13] Rosen J, Hutchings G S, Jiao F. Ordered mesoporous cobalt oxide as highly efficient oxygen evolution catalyst[J]. *Journal of the American Chemical Society,* 2013, *135(11): 4516-4521.*

[14] Chen J, Chen C, Qin M, et al. Reversible hydrogen spillover in Ru-WO3-x enhances hydrogen evolution activity in neutral pH water splitting[J]. *Nature Communications,* 2022, *13(1): 5382.*

[15] Shen B, Feng Y, Wang Y, et al. Holey MXene nanosheets intimately coupled with ultrathin Ni-Fe layered double hydroxides for boosted hydrogen and oxygen evolution reactions[J]. *Carbon*, 2023, *212: 118141.*

[16] Zhao X, Ding X, Xia Y, et al. Coupling-effect-induced acceleration of electron transfer for α-$Ni(OH)_2$ with enhanced oxygen evolution reaction activity[J]. *ACS Applied Nano Materials,* 2018, *1(4): 1476-1483.*

[17] Liu Z, Guo Z, He H, et al. Interface regulation of Pt quantum dots doped nickel phosphide and cobalt hydroxide to promote electrocatalytic overall water splitting[J]. *International Journal of Hydrogen Energy,* 2022, *47(97): 40986-40998.*

[18] Cheng R, Min Y, Li H, et al. Electronic structure regulation in the design of low-cost efficient electrocatalysts: From theory to applications[J]. *Nano Energy,* 2023, *115: 108718.*

[19] Zhang Y, Lin Y, Duan T, et al. Interfacial engineering of heterogeneous catalysts for electrocatalysis[J]. *materials today,* 2021, *48: 115-134.*

[20] Lipatov A, Alhabeb M, Lukatskaya M R, et al. Effect of synthesis on quality, electronic properties and environmental stability of individual monolayer $Ti_3C_2T_x$ MXene flakes[J]. *Advanced Electronic Materials,* 2016, *2(12): 1600255.*

[21] Li L, Yu D, Li P, et al. Interfacial electronic coupling of ultrathin transition-metal hydroxide nanosheets with layered MXenes as a new prototype for platinum-like hydrogen evolution[J]. *Energy & Environmental Science,* 2021, *14(12): 6419-6427.*

[22] Fang Z, Peng C, Zhou Q, et al. Electrocatalytic hydrogen peroxide production: advances, challenges, and future perspectives[J]. The Chemical Record, 2025, 25(9): e202500066.

[23] Zhang S, Xu X, Liu X, et al. Heterointerface optimization in a covalent organic framework-on-MXene for high-performance capacitive deionization of oxygenated saline water[J]. *Materials Horizons,* 2022, *9(6): 1708-1716.*

[24] Guo D, Ming F W, Shinde D B, et al. Covalent assembly of two‐dimensional COF‐on‐MXene heterostructures enables fast charging lithium hosts[J]. *Advanced Functional Materials,* 2021, *31(25): 2101194.*

[25] Li Y, Bu J, Sun Y, et al. Efficient degradation of norfloxacin by synergistic activation of PMS with a three-dimensional electrocatalytic system based on Cu-MOF[J]. Separation and Purification Technology, 2025, 356: 129945.

[26] Dai L, Ren Y, Li S, et al. Room-temperature synthesis of $Co(OH)_2$/$Mo_2TiC_2T_x$ hetero-nanosheets with interfacial coupling for enhanced oxygen evolution reaction[J]. *Chinese Chemical Letters,* 2025*, 36(4): 109774.*

[27] Solangi M Y, Lakhair A A, Dayo F Z, et al. $Ti_3C_2T_x$ MXene coupled $Co(OH)_2$: a stable electrocatalyst for the hydrogen evolution reaction in alkaline media[J]. *RSC Sustainability,* 2024*, 2(11): 3424-3435.*

[28] Xu T, Wang J, Cong Y, et al. Ternary BiOBr/TiO_2/$Ti_3C_2T_x$ MXene nanocomposites with heterojunction structure and improved photocatalysis performance[J]. *Chinese Chemical Letters,* 2020, *31(4): 1022-1025.*

[29] Park T H, Yu S, Koo M, et al. Shape-adaptable 2D titanium carbide (MXene) heater[J]. *ACS nano,* 2019, *13(6): 6835-6844.*

[30] Li T, Rong J, Liu S, et al. In-situ growth of 3D porous tunnel-like NaV6O15@ C on carbon cloth as high-capacity zinc ion battery cathode[J]. Journal of Alloys and Compounds, 2023, 965: 171418.

[31] Vazquez-Santos M B, Geissler E, Laszlo K, et al. Comparative XRD, Raman, and TEM study on graphitization of PBO-derived carbon fibers[J]. The Journal of Physical Chemistry C, 2012, 116(1): 257-268.

[32] Lu C, Li A, Li G, et al. S‐decorated porous Ti_3C_2 MXene combined with in situ forming Cu2Se as effective shuttling interrupter in Na–Se batteries [J]. *Advanced Materials,* 2021, *33(33): 2008414.*

[33] Gawali S R, Gandhi A C, Gaikwad S S, et al. Role of cobalt cations in short range antiferromagnetic Co_3O_4 nanoparticles: a thermal treatment approach to affecting phonon and magnetic properties[J]. *Scientific reports,* 2018, *8(1): 249.*

[34] Yan L, Zhang B, Zhu J, et al. Chestnut-like copper cobalt phosphide catalyst for all-pH hydrogen evolution reaction and alkaline water electrolysis [J]. *Journal of Materials Chemistry A,* 2019, *7(23): 14271-14279.*

[35] Wu Y, Xiong W, Wang Z, et al. Self-assembled MXene-based Schottky-junction upon Transition metal oxide for regulated tumor microenvironment and enhanced CDT/PTT/MRI activated by NIR irradiation[J]. *Chemical Engineering Journal*, 2022, *427: 131925.*

[36] Zhang B, Shan J, Wang X, et al. Ru/Rh cation doping and oxygen‐vacancy engineering of FeOOH nanoarrays@ $Ti_3C_2T_x$ MXene heterojunction for highly efficient and stable electrocatalytic oxygen evolution[J]. *Small,* 2022, *18(25): 2200173.*

[37] Yang X, Xu C, Li S, et al. Thermal treatment for promoting interfacial interaction in Co-BDC/$Ti_3C_2T_x$ hybrid nanosheets for hybrid supercapacitors [J]. *Journal of colloid and interface science,* 2022, *617: 633-640.*

[38] Xiao T, Jin J, Zhang Y, et al. Rational construction of 2D/2D $Ti_3C_2T_x$/NiCo MOF heterostructure for highly efficient Li^+ storage[J]. *Electrochimica Acta*, 2022, *427: 140851.*

[39] Liu Z, Chen J, Que M, et al. 2D $Ti_3C_2T_x$ MXene/MOFs composites derived CoNi bimetallic nanoparticles for enhanced microwave absorption[J]. *Chemical Engineering Journal,* 2022, *450: 138442.*

[40] Liu Y, Zhang M, Hu D, et al. Ar plasma-exfoliated ultrathin NiCo-layered double hydroxide nanosheets for enhanced oxygen evolution[J]. *ACS Applied Energy Materials,* 2019, *2(2): 1162-1168.*

[41] Lin J, Zheng X, Wang Y, et al. Rational construction of core–shell Ni3S2@Ni(OH)2 nanostructures as battery-like electrodes for supercapacitors[J]. Inorganic Chemistry Frontiers, 2018, 5(8): 1985-1991.

[42] Halim J, Cook K M, Naguib M, et al. X-ray photoelectron spectroscopy of select multi-layered transition metal carbides (MXenes)[J]. Applied Surface Science, 2016, 362: 406-417.

[43] Chen L, Ma F, An Y, et al. Self-Supporting FeOOH/NiFe-LDH Heterostructures with a Built-In Electric Field for Efficient and Durable Alkaline Seawater Oxidation[J]. The Journal of Physical Chemistry Letters, 2026, 17(7): 2118-2127

[44] 44]. Li Z, Jiang Z, Zhu W, et al. Facile preparation of CoSe2 nanovesicle derived from ZIF-67 and their application for efficient water oxidation[J]. Applied Surface Science, 2020, 504: 144368.

[45] Newville M. IFEFFIT: interactive XAFS analysis and FEFF fitting[J]. *Journal of Synchrotron Radiation,* 2001, *8(2): 322-324.*

[46] Ravel B, Newville M. ATHENA, ARTEMIS, HEPHAESTUS: data analysis for X-ray absorption spectroscopy using IFEFFIT[J]. *Journal of Synchrotron Radiation*, 2005, 12(4): *537-541.*

[47] Funke H, Scheinost A C, Chukalina M. Wavelet analysis of extended x-ray absorption fine structure data[J]. *Physical Review B*, 2005, 71(9): 094110.

[48] Fei H, et al. Atomic cobalt on nitrogen-doped graphene for hydrogen generation[J]. Nature Communications, 2015, 6: 8668.

[49] Li Z, Liu D, Lu X, et al. Boosting oxygen evolution of layered double hydroxide through electronic coupling with ultralow noble metal doping[J]. Dalton Transactions, 2022, 51(4): 1527-1532.

[50] Zitolo A, et al. Identification of catalytic sites for oxygen reduction in iron- and nitrogen-doped graphene materials[J]. Nature Materials, 2015, 14(9): 937-942.

[51] Qin D, Liu C, Song K, et al. Bioinspired silk fibroin/poly-acrylic acid high-performance hydrogel sensors with micro-architecture prepared by rapid polymerization via TA-Fe3O4@ MXene catalytic system[J]. Chemical Engineering Journal, 2025: 170300.

[52] Jiang H, et al. Tracking structural self-reconstruction and identifying true active sites toward cobalt oxychloride pre-catalyst of oxygen evolution reaction[J]. *Advanced Materials,* 2019, *31(19): 1805127.*

[53] Ye L, Ding Y, Niu X, et al. Unraveling the crucial contribution of additive chromate to efficient and stable alkaline seawater oxidation on Ni-based layered double hydroxides[J]. *Journal of Colloid and Interface Science,* 2024, *665: 240-251.*

[54] Wang Z, Niu X, Ye L, et al. Boron modification promoting electrochemical surface reconstruction of NiFe-LDH for efficient and stable freshwater/seawater oxidation catalysis[J]. *Journal of Colloid and Interface Science*, 2024, *668: 607-617.*

Electronic Supplementary Material

Ti_3C_2 MXene folded nanosheets with $Co(OH)_2$ integrated on carbon cloth for enhanced oxygen evolution performance

Bingbing Hang[1], Xilin Zhang[1,2], Qingfang Chang[1,2,*] Runmin Li[3], Qian Bai[3], Shuai Li[4,*], Xi Liu[5], and Jiajing Pei[5,*]

[1] *School of Physics, Henan Normal University, Xinxiang 453007, China*
[2] *Key Laboratory of Yellow River and Huai River Water Environmental and Pollution Control, Ministry of Education, School of Environment, Henan Normal University, Xinxiang 453007, China*
[3] *Energy & Catalysis Center, School of Materials Science and Engineering, Beijing Institute of Technology, Beijing 100081, China*
[4] *College of Environmental Science and Engineering, North China Electric Power University, Beijing 102206, China*
[5] *State Key Laboratory of High-efficiency Utilization of Coal and Green Chemical Engineering, College of Chemistry and Chemical Engineering, Ningxia University, Yinchuan 750021, China*

Received: 6 April 2026; **Revised:** 11 May 2026; **Accepted:** 13 May 2026

Address correspondence to Qingfang Chang, qingfangchang@htu.edu.cn; Shuai Li, 053_lishuai@163.com; Jiajing Pei, pjj@nxu.edu.cn

Supporting information to https://doi.org/10.26599/NR.2026.94908840

Chemicals and regents

All chemical reagents were of analytical grade and used without further purification. Cobalt nitrate hexahydrate ($Co(NO_3)_2·6H_2O$), urea, ammonium fluoride (NH_4F), and potassium hydroxide (KOH) were purchased from Sinopharm Chemical Reagent Co., Ltd. Titanium aluminum carbide (Ti_3AlC_2, 400 mesh) was obtained from Jilin 11 Technology Co., Ltd. Lithium fluoride (LiF, 99.0%) and hydrochloric acid (HCl, 36–38%) were sourced from Shanghai Maclin Biochemical Technology Co., Ltd. Carbon cloth (CC, TGP-H-060) was procured from Suzhou Sinero Technology Co., Ltd. Methanol and ethanol were supplied by Sinopharm Group Chemical Reagent Co., Ltd. Ruthenium(IV) oxide (RuO_2) and Nafion (5 wt%) were purchased from Shanghai Maclin Biochemical Technology Co., Ltd. and Shanghai Hesen Electric Co., Ltd., respectively. Deionized (DI) water with a resistivity of 18.2 MΩ·cm was produced using a Purite Neptune purification system.

Material synthesis

Synthesis of $Ti_3C_2T_X$

Monolayer $Ti_3C_2T_X$ MXene was obtained by selectively etching metallic Al from Ti_3AlC_2 using a mixed acid etchant. 2 mL of 28.4 M HF (48%), 9 mL of 12 M HCl (37%), and 4.5 mL of deionized water were mixed in a 50 mL PTFE container and stirred for 10 min. Then, 0.5 g of Ti_3AlC_2 was gradually added at 35 °C, and the mixture was stirred for 25 h, followed by 5 h stirring at room temperature to fully etch the Al layer. The product was washed with DI water and centrifuged at 3234 Relative Centrifugal Force for 5 min repeatedly until the pH exceeded 6.

To obtain few-layer $Ti_3C_2T_X$, the multilayer sediment was redispersed in 12.5 mL DI water. Meanwhile, 0.8 g LiF was dissolved in 12.5 mL DI water and stirred for 5 min. The two solutions were mixed and bubbled with N_2 at 65 °C for 1 h. The dispersion was centrifuged at 3234 RCF for 5, 10, 15, and 20 min sequentially. After redispersing in water and vortexing for 20 min, the mixture was centrifuged at 2380 RCF for 30 min, and the supernatant containing few-layer $Ti_3C_2T_X$ was collected.

Synthesis of $Co(OH)_2$/CC Nanosheet Arrays.

Carbon cloth was ultrasonicated in acetone, ethanol, and DI water for 30 min each, then dried at 60 °C for 5 h. It was then immersed in concentrated nitric acid at 60 °C for 1 h and at room temperature for 2.5 h, rinsed thoroughly, and dried. 1.7461 g $Co(NO_3)_2·6H_2O$ and 1.6816 g urea ($(CONH_2)_2$) were dissolved in 50 mL DI water and stirred for 60 min. Electrodeposition was carried out in a three-electrode system with treated carbon cloth (1×1.2 cm^2) as the working electrode, Pt sheet as the counter electrode, at a constant potential of -0.9 V for 10 min (repeated twice). After ultrasonically rinsing with deionized water and ethanol, the product was dried in an oven at 60 °C to obtain $Co(OH)_2$/CC.

Preparation of MXene@$Co(OH)_2$/CC Electrode.

30 mg of as-prepared few-layer $Ti_3C_2T_X$ MXene was dispersed in 30 mL DI water and sonicated to form a homogeneous solution. $Co(OH)_2$/CC was immersed into the MXene dispersion to ensure sufficient contact, then rapidly dried in a vacuum oven at 80 °C for several minutes. This immersion-drying cycle was repeated several times to obtain MXene@$Co(OH)_2$/CC.

Characterization.

The The morphology of the samples was characterized using scanning electron microscopy (SEM, QUANTA FEG250), transmission electron microscopy (TEM), and high-resolution transmission electron microscopy (HRTEM, JEOL JEM 2100Plus). Energy-dispersive X-ray (EDX) analysis and corresponding elemental distribution data were obtained using an X-ray spectrometer coupled to the transmission electron microscope. X-ray diffraction (XRD) patterns were recorded on a Rigaku Ultima IV diffractometer with Cu Kα radiation (λ = 0.15418 nm) over 5–80°. The instrument employed for XPS analysis is a Thermo Fisher ESCALAB 250Xi X-ray photoelectron spectrometer. It utilizes an aluminum Kα X-ray excitation source (hν = 1486.6 eV) to measure the surface chemical composition of samples. The binding energy of all XPS spectra is calibrated based

on the C1s line at 284.8 eV. Raman spectra were collected on a T6400 spectrometer (Jobin Yvon) with a 532 nm laser. The Co K-edge X-ray absorption data were collected at BL1W1B station in BSRF. The radiation was monochromatized by a Si (111) double-crystal monochromator. The intensity of the incident X-ray was monitored by an ion chamber (I_0) in front of the sample. Solid samples were placed in an aluminum sample holder sealed with Kapton tape. Data were collected as fluorescence excitation spectra with a Lytle detector. The samples were pelletized as disks of 13 mm diameter with 1 mm thickness using graphite powder as binder. The spectra of the references were recorded in transmission mode using an ionization chamber. All data were collected at room temperature.

XAFS data processing

The acquired EXAFS data were processed according to the standard procedures using the Athena and Artemis implemented in the IFEFFIT software packages. The fitting detail is described below: The acquired EXAFS data were processed according to the standard procedures using the ATHENA module implemented in the IFEFFIT software packages. The EXAFS spectra were obtained by subtracting the post-edge background from the overall absorption and then normalizing with respect to the edge-jump step. Subsequently, the χ(k) data of Fourier transformed to real (R) space using a hanning windows (dk=1.0 $Å^{-1}$) to separate the EXAFS contributions from different coordination shells. To obtain the quantitative structural parameters around central atoms, least-squares curve parameter fitting was performed using the ARTEMIS module of the IFEFFIT software packages. The following EXAFS equation was used:

$$\chi(k)=\sum_j \frac{N_j S_o^2 F_j(k)}{k R_j^2}\exp[-2k^2\sigma_j^2]\exp[\frac{-2R_j}{\lambda(k)}]\sin[2kR_j+\phi_j(k)] \quad (1)$$

S_0^2 is the amplitude reduction factor, $F_j(k)$ is the effective curved-wave backscattering amplitude, Nj is the number of neighbors in the j^{th} atomic shell, R_j is the distance between the X-ray absorbing central atom and the atoms in the j^{th} atomic shell (backscatterer), λ is the mean free path in Å, $\phi_j(k)$ is the phase shift (including the phase shift for each shell and the total central atom phase shift), σ_j is the DebyeWaller parameter of the j^{th} atomic shell (variation of distances around the average R_j). The functions $F_j(k)$, λ, and $\phi_j(k)$ were calculated with the ab initio code FEFF8.2. The additional details for EXAFS simulations are given below. The coordination numbers of model samples (Pt foil) were fixed as the nominal values. The obtained S_0^2 was fixed in the subsequent fitting of atomically dispersed Pt samples. While the internal atomic distances R, Debye-Waller factor σ^2, and the edge-energy shift ΔE_0 were allowed to run freely.

Electrochemical tests for OER.

OER experiments employed a three-electrode configuration with a CHI 660E workstation at ambient conditions. The electrochemical cell consisted of: (1) catalyst-coated carbon cloth (1 cm^2 geometric area) as the working electrode, (2) graphite counter electrode, and (3) Hg/HgO reference electrode. MXene@Co $(OH)_2$/CC was cut into 1×1.2 cm^2 (effective working area: 1 cm^2) and fixed on a Pt sheet ensure tight contact and minimize contact resistance. Current densities were normalized to the electrode's geometric surface area (1 cm^2). The HgO reference electrode was calibrated in O_2-saturated 1 M KOH using a symmetric Pt electrode system. All reported potentials were referenced to the RHE using the equation:

$$E_{RHE} = E_{Hg/HgO} + 0{:}059 \times pH + 0.098$$

Before linear sweep voltammetry (LSV), the electrode was activated by cyclic voltammetry (CV) at 50 $mV{\cdot}s^{-1}$ for 30 cycles. LSV curves were recorded at 1 $mV{\cdot}s^{-1}$. The electrochemical double-layer capacitance (Cdl) was measured by CV at scan rates of 5, 6, 7, 8, 9 $mV{\cdot}s^{-1}$ in the non-Faradaic region (0.25-0.35 V vs. RHE) to evaluate the electrochemically active surface area (ECSA). Long-term stability was evaluated by chronopotentiometry at a constant current density of 10 $mA{\cdot}cm^{-1}$ without iR compensation. Electrochemical impedance spectroscopy (EIS) was performed at 1.58 V vs. RHE. Commercial RuO_2 loaded on CC was tested under identical conditions for comparison. All LSV curves were corrected by subtracting the background current of bare carbon cloth.

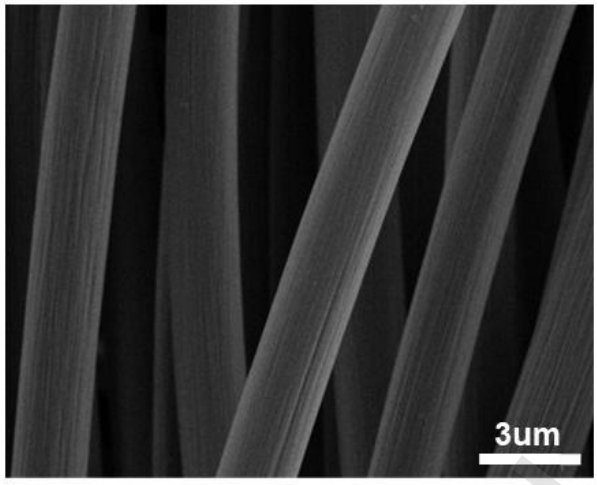

Figure S1. SEM image of CC.

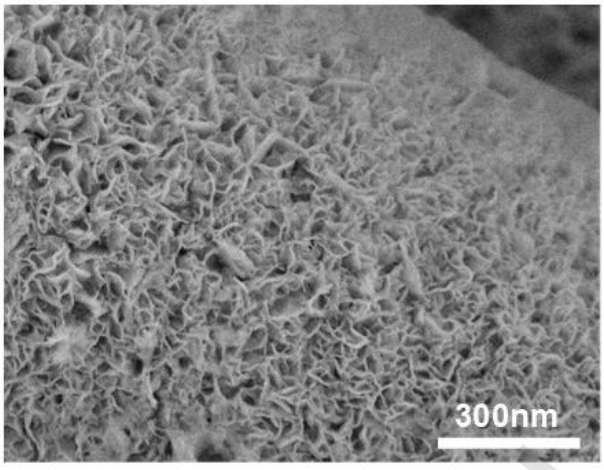

Figure S2. SEM image of $Co(OH)_2$.

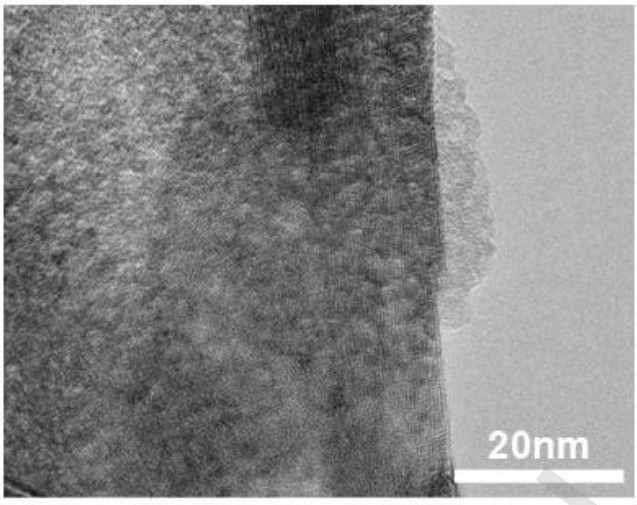

Figure S3. HRTEM image at high magnification of MXene@$Co(OH)_2$/CC.

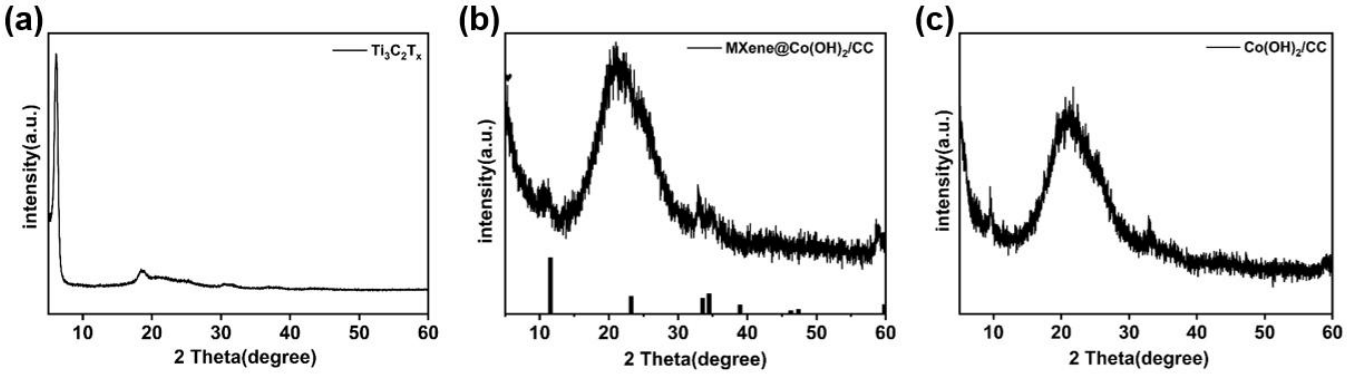

Figure S4. (a) XRD pattern of $Ti_3C_2T_x$; (b) XRD pattern of MXene@$Co(OH)_2$/CC; (c) XRD pattern of $Co(OH)_2$/CC, The broad peak at 25.6° is assigned to the C(002) reflection of the carbon cloth substrate, consistent with typical reports for similar materials. The slight deviation from the standard graphite value (~26.5°) is due to the inherently lower graphitization degree of commercial carbon cloth, as established in carbon materials science .

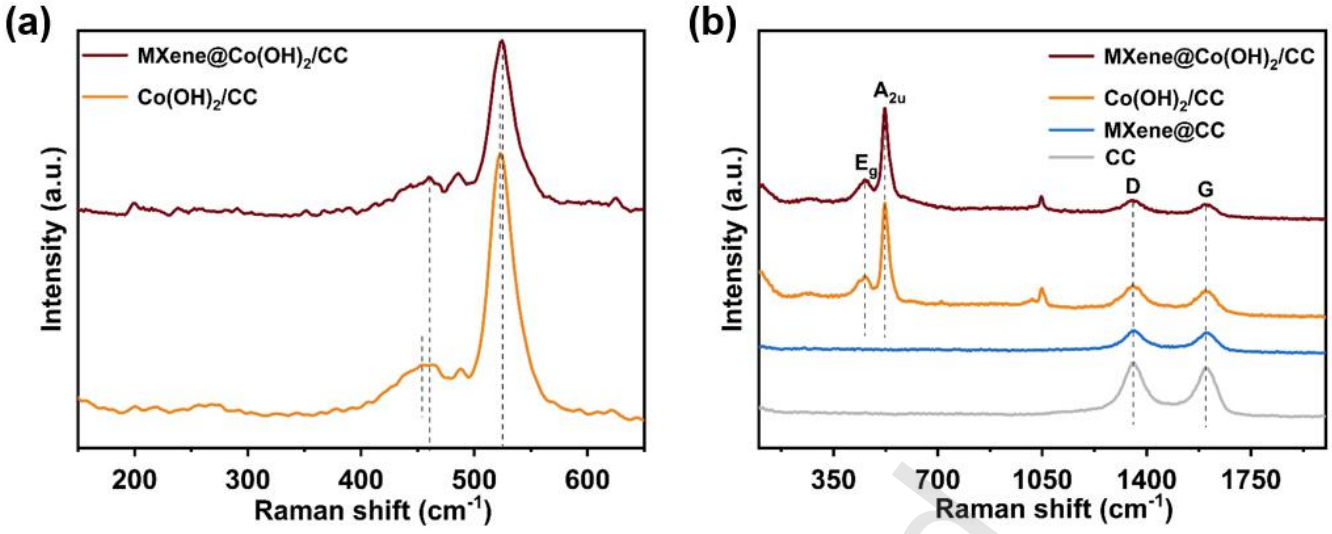

Figure S5. (a) Raman spectra of MXene@$Co(OH)_2$/CC and $Co(OH)_2$/CC; (b) Raman spectra of MXene@$Co(OH)_2$/CC、$Co(OH)_2$/CC、MXene@CC、CC.

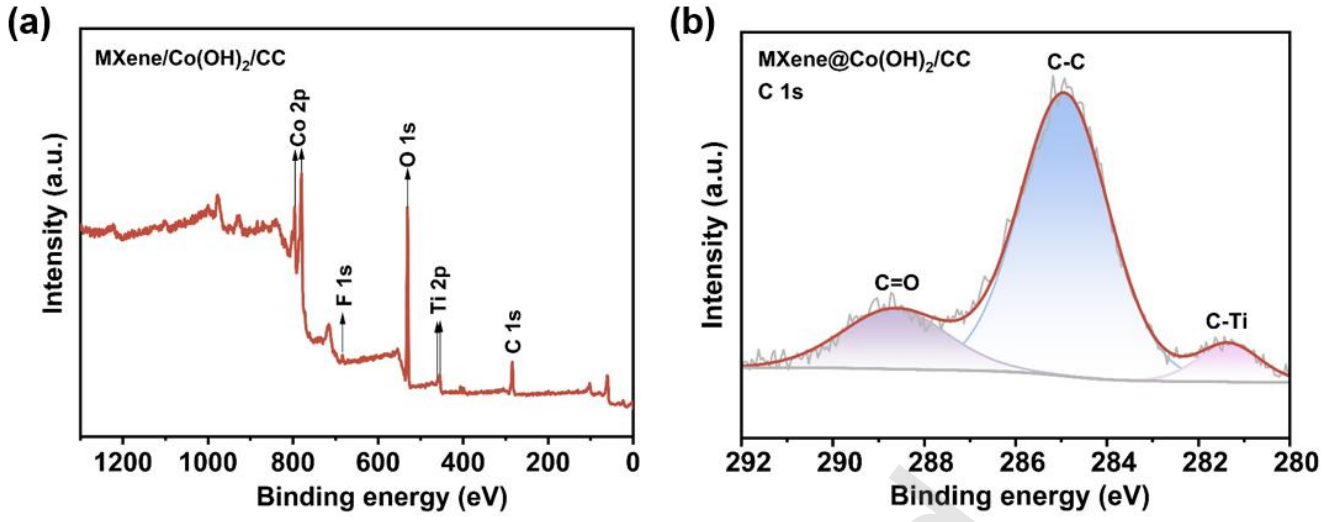

Figure S6. (a) XPS curves of MXene/$Co(OH)_2$/CC all curves; (b) XPS spectra of C 1s.

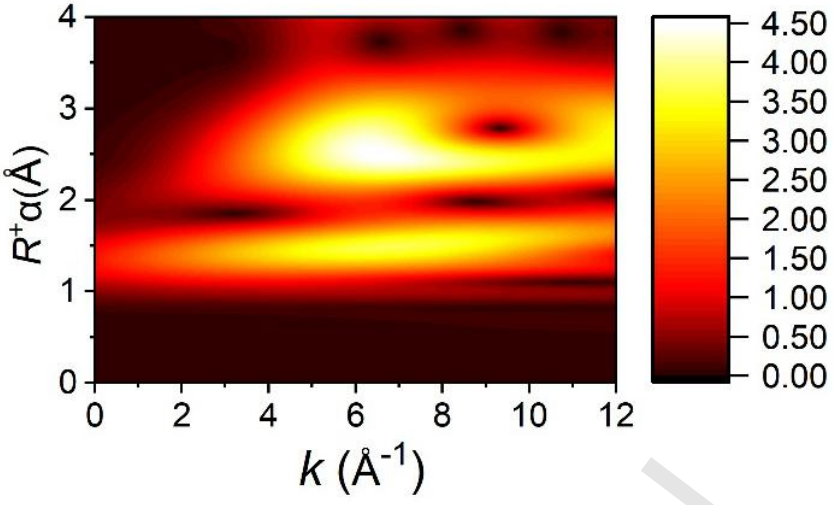

Figure S7. The WT-EXAFS plots of Co_3O_4.

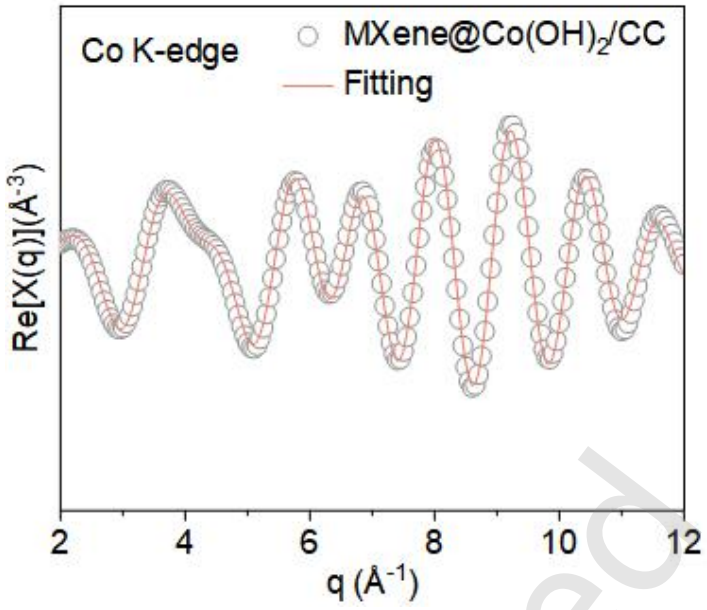

Figure S8. The q-space EXAFS fitting curve of MXene@$Co(OH)_2$/CC.

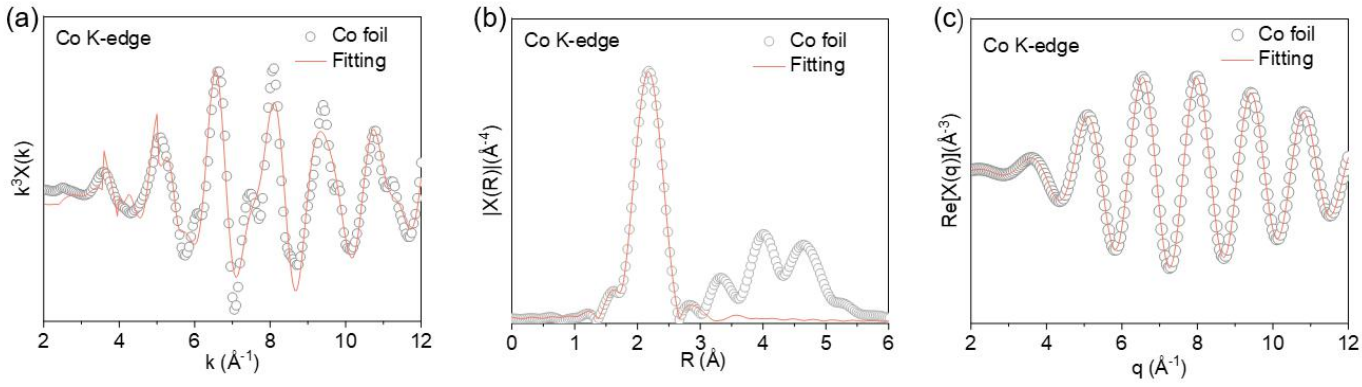

Figure S9. The (a) k-space EXAFS fitting curve ; (b) R-space EXAFS fitting curve; (c) q-space EXAFS fitting curve of Co foil.

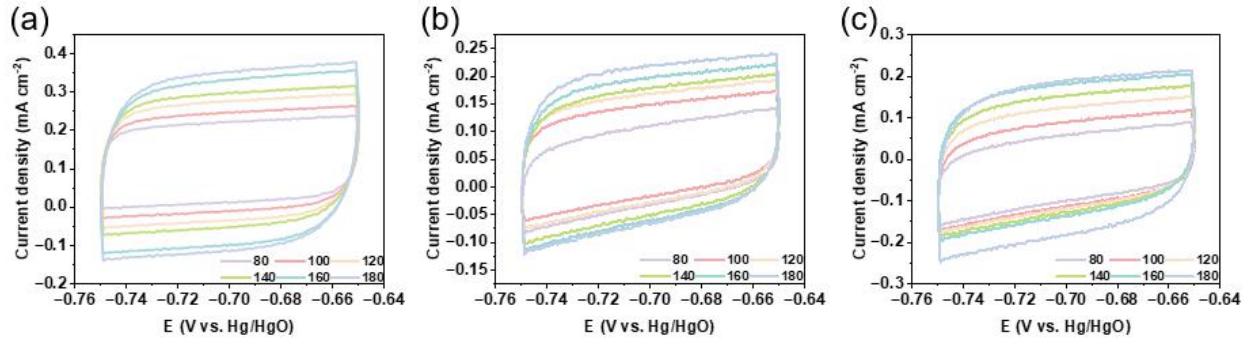

Figure S10. Figure S10. CVs performed for (a) MXene@Co(OH)2/CC; (b) Co(OH)2/CC; (c) CC, Linear fitting of the capacitive current densities versus scan rates for the as-prepared catalysts. The measurements were performed in the non-faradaic potential range of -0.75 to -0.65 V vs. Hg/HgO.

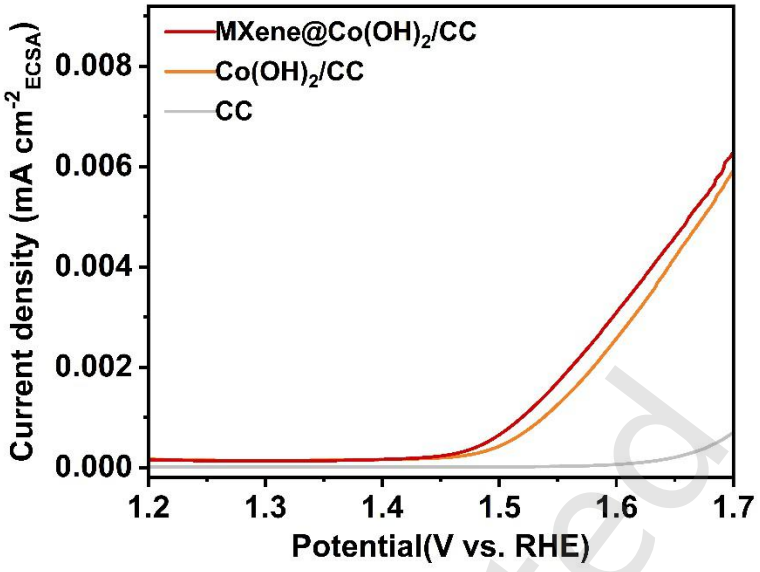

Figure S11. LSV curves normalized by ECSA based on the impact of ECSA.

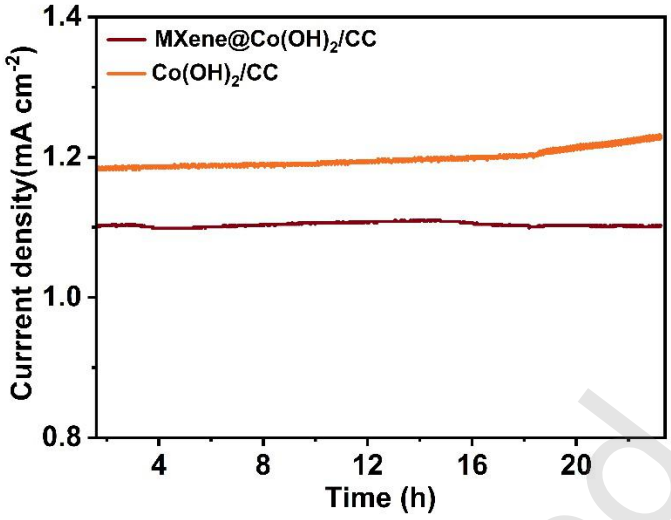

Figure S12. Stability of MXene@$Co(OH)_2$/CC and $Co(OH)_2$/CC for 23 h at 10 mA cm^{-2} current density.

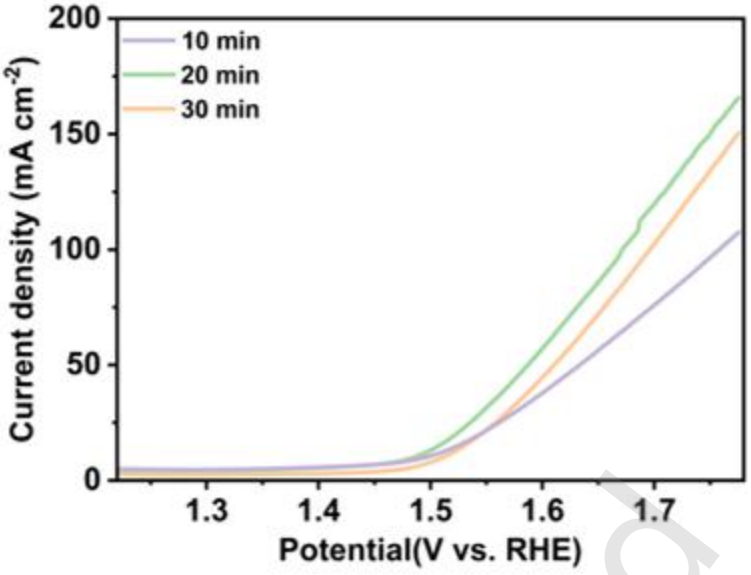

Figure S13. Chronopotentiometry curves of MXene@$Co(OH)_2$/CC.

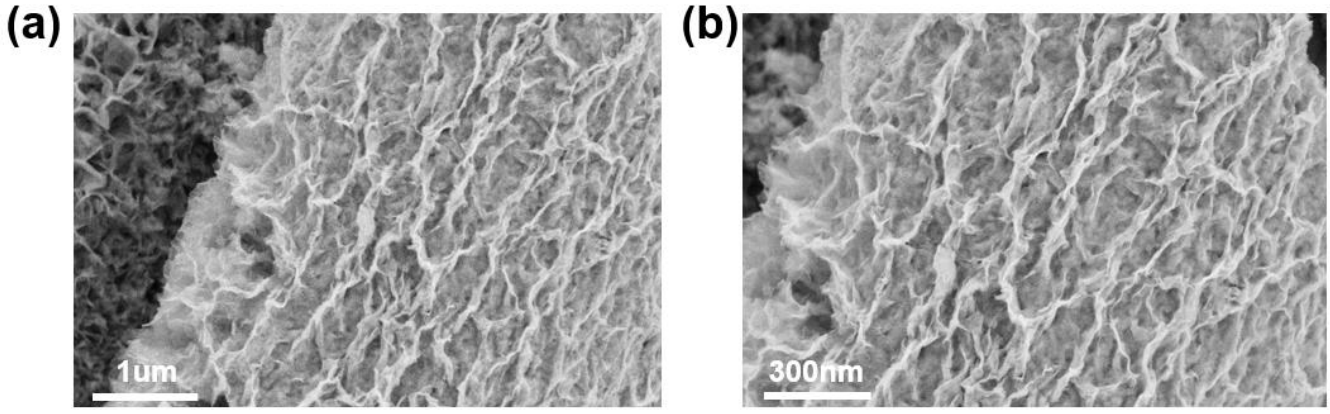

Figure 14 SEM images of MXene@$Co(OH)_2$ after stability test: (a) low-magnification morphology; (b) high-magnification morphology.

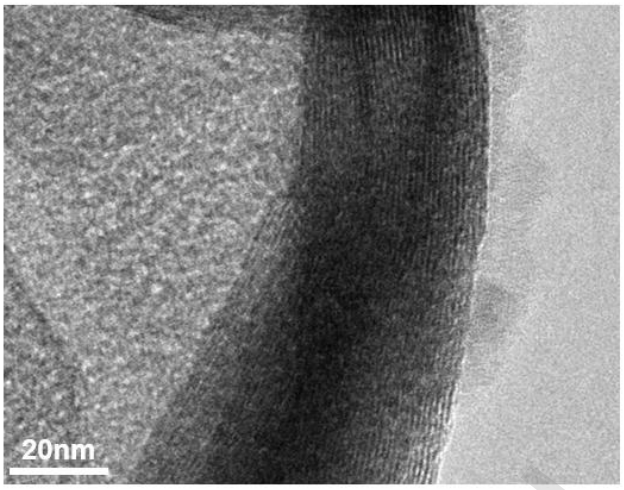

Figure 15. HRTEM image of MXene@$Co(OH)_2$ after stability test.

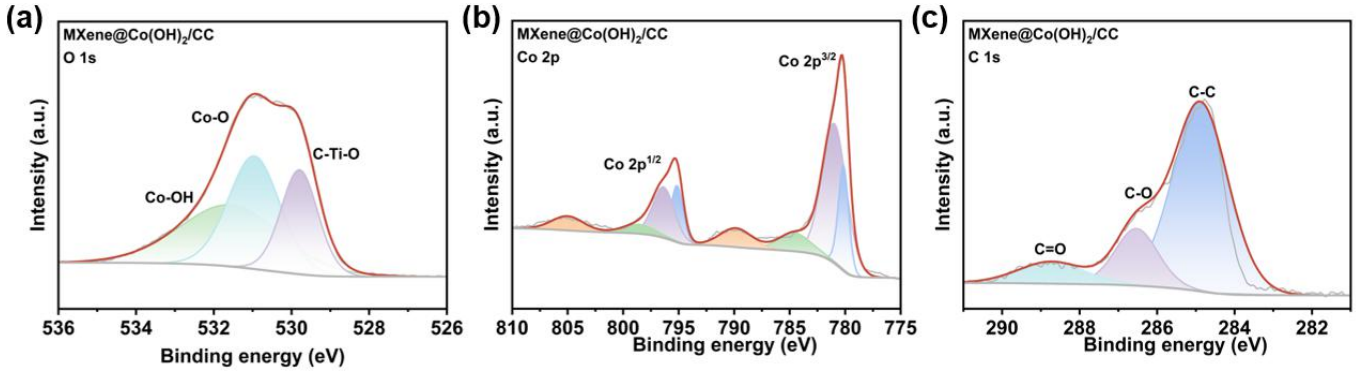

Figure S16. High-resolution XPS spectra of the MXene@$Co(OH)_2$/CC electrode after stability test. (a) O 1s spectrum; (b) Co 2p spectrum; (c) C 1s spectrum.

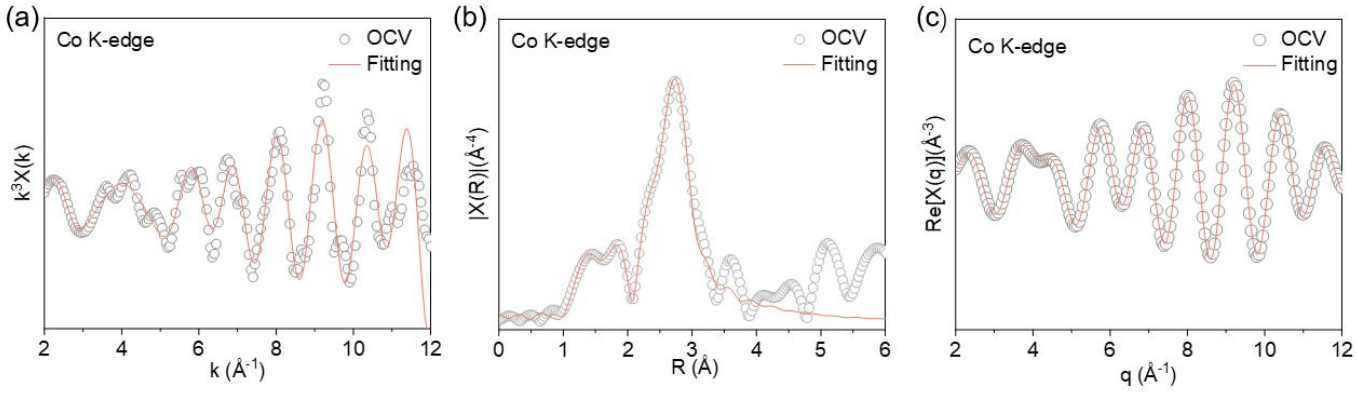

Figure S17. (a) k-space, (b) R-space, (c) q-space at OCV of MXene@$Co(OH)_2$/CC.

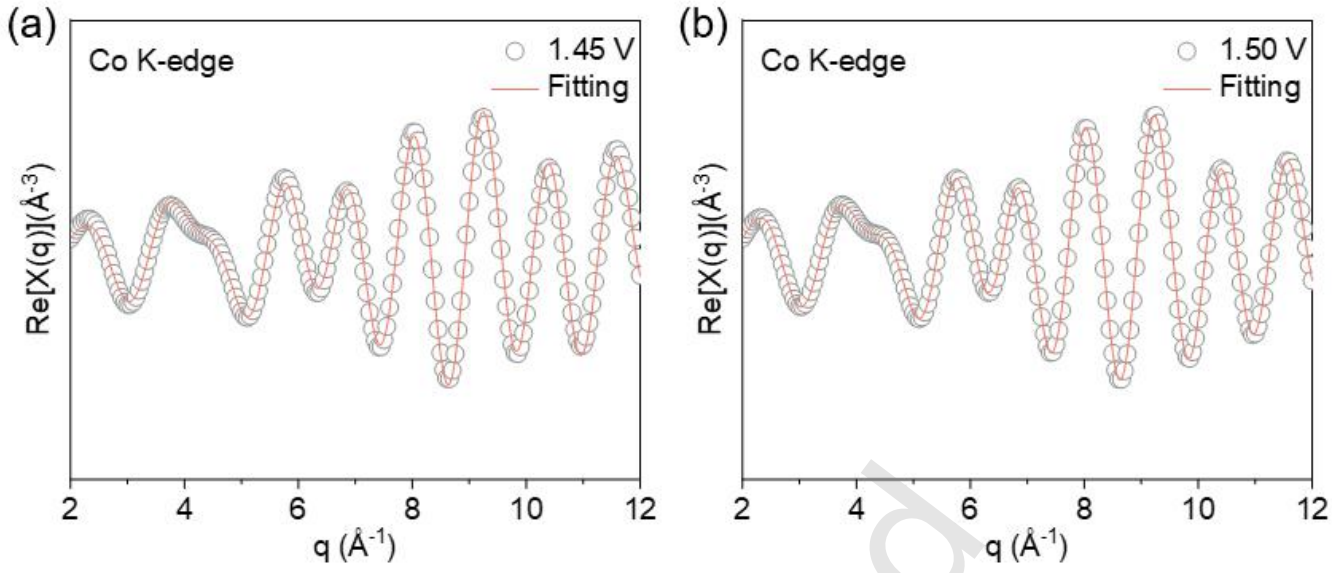

Figure S18. (a) The q space Fitting curve at 1.45 V (vs. RHE); (b) The q space Fitting curve at 1.50 V (vs. RHE).

Table S1. The EXAFS fitting result of Co K-edge. (S_0^2 = 0.86)

Sample	Path	CN	R(Å)	$\sigma^2(10^{-3}Å^2)$	ΔE_0(eV)	R factor
Co foil	Co-Co	12*	2.47±0.01	4.9±0.3	6.5±0.2	0.006
MXene@Co(OH)$_2$	Co-O	1.9±0.4	1.93±0.02	4.2±0.5	2.6±0.3	0.011
OCV	Co-O	2.4±0.1	1.94±0.02	4.1±0.2	2.2±0.3	0.012
1.45 V	Co-O	2.3±0.4	1.92±0.01	4.5±0.3	2.5±0.3	0.010
1.50 V	Co-O	2.6±0.3	1.90±0.01	4.6±0.5	2.4±0.3	0.013

Table S2. Equivalent circuit for the EIS measurements and fitted resistance data of OER.

Catalysts	Rs [Ω]	Rct [Ω]
MXene@$Co(OH)_2$/CC	1.236	1.68
$Co(OH)_2$/CC	1.299	2.188
MXene@CC	1.22	204.5

Table S3 Comparison of OER performance of the present work with the reported related catalysts in 1.0 mol/L KOH solution.

	lectrocatalyst	Electrolyte	η(mV)@ 10mA/cm^2	Tafel slope (mV.dec^{-1})	Reference
1	$Co(OH)_2/Mo_2TiC_2T_x$-3	1 mol/L KOH	283	80	[1]
2	FeCo-LDH/MXene	1 mol/L KOH	268	85	[2]
3	$Co(OH)_2$/S-Ti_3C_2Tx	1 mol/L KOH	207	86.91	[3]
4	CoFeLDH-Ti_3C_2Tx	1 mol/L KOH	301	43	[4]
5	S-CoLaLDH/MXene	1 mol/L KOH	303	57	[5]
6	NiFeCo-LDH/TiO_2/MXenes	1 mol/L KOH	320	98.4	[6]
7	Co-LDH@MXenes	1 mol/L KOH	330	82	[7]
8	Co_3O_4 QDs/MXene	1 mol/L KOH	340	63.97	[8]
9	$NiCo_2$(OH)x/MXene	1 mol/L KOH	268	87	[9]
10	NiFeCo0.75 LDH@Ti_3C_2Tx	1 mol/L KOH	258	44.78	[10]
11	NiFe-LDH@carbon	1 mol/L KOH	340	67	[11]
12	α-$Co(OH)_2$/HNFs	1 mol/L KOH	310	68.9	[12]

References

[1].*Dai L, Ren Y, Li S, et al. Room-temperature synthesis of $Co(OH)_2/Mo_2TiC_2T_x$ hetero-nanosheets with interfacial coupling for enhanced oxygen evolution reaction[J]. Chinese Chemical Letters, 2025, 36(4): 109774.*

[2].*Tian M, Jiang Y, Tong H, et al. MXene-supported FeCo-LDHs as highly efficient catalysts for enhanced electrocatalytic oxygen evolution reaction[J]. ChemNanoMat, 2020, 6(1): 154-159.*

[3].*Pei Y, Gu M, Wang H, et al. Synergistic Enhancement of Oxygen Evolution by S-$Ti_3C_2T_x$ MXene Folded Nanosheets Supported by Cobalt Hydroxide Nanoparticles[J]. ACS Applied Nano Materials, 2024, 7(17): 20544-20552.*

[4].*Sheng J, Kang J, Jiang P, et al. Guided heterostructure growth of CoFe LDH on $Ti_3C_2T_x$ MXene for durably high oxygen evolution activity[J]. Small, 2025, 21(3): 2404927.*

[5].*Lv G, Lu Q, Ma Z, et al. Synthesis of a sulfur-doped CoLaLDH/MXene composite as an efficient electrocatalyst for the oxygen evolution reaction in alkaline medium[J]. New Journal of Chemistry, 2025, 49(19): 7794-7803.*

[6].*Hao N, Wei Y, Wang J, et al. In situ hybridization of an MXene/TiO_2/NiFeCo-layered double hydroxide composite for electrochemical and photoelectrochemical oxygen evolution[J]. RSC advances, 2018, 8(37): 20576-20584.*

[7].*Li C, Dai Z, Liu W, et al. A self-sacrifice template strategy to synthesize Co-LDH/MXene for lithium-ion batteries[J]. Chemical Communications, 2021, 57(86): 11378-11381.*

[8].*Zhou H, Sun Y, Yang H, et al. Co_3O_4 Quantum Dots Intercalation Liquid-Crystal Ordered-Layered-Structure Optimizing the Performance of 3D-Printing Micro-Supercapacitors[J]. Advanced Science, 2023, 10(33): 2303636.*

[9].*Xu J, Zhong X, Wu X, et al. Optimizing the electronic spin state and delocalized electron of $NiCo_2(OH)_x$/MXene composite by interface engineering and plasma boosting oxygen evolution reaction[J]. Journal of Energy Chemistry, 2022, 71: 129-140.*

[10].*Dong W, Wei B, Zhang L, et al. Co doped NiFe LDH nanosheets in situ anchored on MXene for the highly efficient oxygen evolution reaction in water splitting[J]. CrystEngComm, 2025, 27(24): 4147-4159.*

[11].*Hu H, Wageh S, Al-Ghamdi A A, et al. NiFe-LDH nanosheet/carbon fiber nanocomposite with enhanced anionic dye adsorption performance[J]. Applied Surface Science, 2020, 511: 145570.*

[12].*Liu H, Guo D, Zhang W, et al. $Co(OH)_2$ hollow nanoflowers as highly efficient electrocatalysts for oxygen evolution reaction[J]. Journal of Materials Research, 2018, 33(5): 568-580.*